THE JOURNAL OF PHYSICAL CHEMISTRY C
Article
Cite This: J. Phys. Chem. C 2018, 122, 25475−25497
pubs.acs.org/JPCC

Consequences of Acid Strength and Diffusional Constraints for Alkane Isomerization and β-Scission Turnover Rates and Selectivities on Bifunctional Metal-Acid Catalysts

Gina Noh,[†] Stacey I. Zones,[‡] and Enrique Iglesia*[,†]

[†]Department of Chemical and Biomolecular Engineering, University of California at Berkeley, Berkeley, California 94720, United States

[‡]Chevron Energy Technology Company, Richmond, California 94801, United States

Supporting Information

ABSTRACT: Crystalline silicates with a given structure but different framework heteroatoms (e.g., Al, Ga, Fe, B in MFI) provide similar confining voids but sites with different acid strength. Their known structure allows systematic mechanistic inquiries into the role of acid strength on reactivity through theory (DFT) and experiments, as illustrated here for isomerization and β-scission of linear and branched alkanes. Stronger acids lead to higher turnover rates for all reactants because of their more stable conjugate anions at ion-pair transition states. As acid strength decreases, β-scission transition states become preferentially stabilized over those for isomerization because of the differences in charge distributions at their carbocations, leading to higher scission selectivities on weaker acids; these findings contradict prevailing paradigms based on observations that reflect the higher proton reactivity in stronger acids, which, in turn, leads to the diffusion-enhanced secondary β-scission of primary isomer products. The small voids in zeotypes lead to high reactivity through transition state stabilization by confinement but also hinder diffusion, leading primary isomers to undergo secondary reactions before egressing into the extracrystalline fluid phase. These diffusional effects lead to the observed high selectivities for β-scission on stronger acids, as shown by reaction-transport formalisms underpinned by experiments that systematically vary intracrystalline proton densities through the gradual desorption of preadsorbed NH_3 titrants during catalysis. These strategies allow intrinsic selectivities (single sojourn at an acid site) to be assessed separately from ubiquitous effects of diffusion-enhanced interconversions. Single-sojourn selectivities are similar on mesoporous and large-pore aluminosilicates (Al-MCM-41, FAU, BEA), reflecting confinement effects that influence isomerization and β-scission transition state carbocations to the same extent. In contrast, single-sojourn selectivities on medium-pore three-dimensional aluminosilicates (SVR, MFI, MEL) are influenced by secondary reactions even as intracrystalline proton densities decrease to very low values, because such reactions are enhanced by diffusional constraints even within a single cage, as a result of the undulating motifs prevalent in these frameworks.

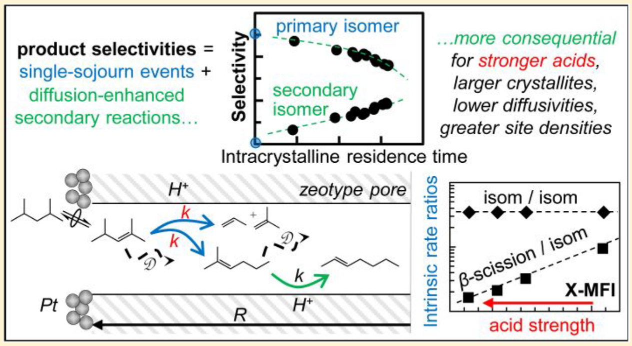

1. INTRODUCTION

Hydrocracking and hydroisomerization processes are used to modify the chain length and backbone structure of alkanes in order to improve the volatility and the combustion and flow properties that render them useful as precursors to fuels and lubricants.[1,2] These reactions are mediated by acid-catalyzed isomerization and β-scission of alkene intermediates formed from alkanes via *in situ* equilibration at a hydrogenation−dehydrogenation metal function.[3−5] Turnover rates and selectivites thus reflect the strength of the acid function. Acid strength is given by the deprotonation energy (DPE), defined as that required to remove a proton from the solid acid to noninteracting distances from its conjugate anion; the acid strength and the reactivity of acid sites in zeotypes can be modified by isomorphous substitution of heteroatoms (Al^{3+}, Ga^{3+}, Fe^{3+}, B^{3+})[6,7] into their silicate frameworks (DPE range: 1167−1214 kJ mol^{-1}) without concomitant changes in the void structure within which the protons reside.[7]

The catalytic reactivity of protons in zeotypes is determined by the effects of acid strength, acting in concert with host−guest confinement effects within voids of molecular dimensions. These confinement effects reflect the stabilization of transition states and intermediates by van der Waals contacts that depend sensitively on the "fit" between the organic guests and the inorganic hosts.[8−10] The small channels and voids in zeotypes are responsible for transition state stabilization, but they can also

Received: August 30, 2018
Revised: October 15, 2018
Published: October 30, 2018

DOI: 10.1021/acs.jpcc.8b08460
J. Phys. Chem. C 2018, 122, 25475−25497

impose significant diffusional constraints; the resulting intracrystalline gradients of the primary products formed can enhance their secondary interconversions as such products diffuse through acid domains before hydrogenation at a metal function. Such diffusion-enhanced secondary reactions become more prevalent on acid domains with more reactive protons and higher volumetric proton densities and for larger crystallites and frameworks with smaller apertures; as a result, transition state stabilization by confinement or by stronger acid sites and these diffusional constraints become inextricably linked and require appropriate mathematical formalisms[8,11] to dissect the separate contributions of acid strength and confinement to the intrinsic reactivity and selectivity of protons (those for a single sojourn at an active site). In the absence of such treatments, phenomenological interpretations of product selectivities in bifunctional catalyst systems have often misinterpreted these diffusional corruptions as effects of acid strength or of transition state confinement on selectivity and reactivity.[12−15]

This study provides a mechanistic assessment of *n*-heptane and 2,4-dimethylpentane isomerization and β-scission rate and selectivity data on mixtures of Pt/SiO_2 with crystallites of H-forms of (1) aluminosilicates of varied pore topology (Al-MCM-41, FAU, SFH, BEA, MEL, MFI, SVR), which have acid sites of similar strength[16,17] that reside in different confining environments and that are used here to investigate the effects of diffusion-enhanced secondary reactions, and (2) zeotypes with the MFI framework but different heteroatom composition and thus acid strength (Al^{3+}, Ga^{3+}, Fe^{3+}, B^{3+}; DPE = 1167−1214 kJ mol^{-1}); the former are used to probe the consequences of void structure on transition state stability and diffusional effects and the latter to examine how and why acid strength influences reactivity and selectivity on protons present within confining voids similar in size and geometry. The effects of reaction−diffusion coupling on measured selectivities are addressed here using insights from density functional theory calculations and a recently developed experimental protocol[8] that monotonically increases the intracrystalline density of accessible protons during 2,4-dimethylpentane reactions by the gradual desorption of preadsorbed NH_3 titrants; such methods permit a rigorous inquiry into the effects of acid strength on single-sojourn product selectivities.

n-Heptane isomerization rate constants (per H^+) decrease exponentially as DPE increases, predominantly because of the less stable conjugate anion at the kinetically relevant ion-pair transition states. The sensitivity of the rate constants to changes in DPE reflects the recovery of a fraction of the ionic component of DPE upon formation of ion-pair transition states, which are stabilized predominantly through Coulombic interactions; O−H bonds in solid acids, in contrast, exhibit significant covalent character, and the energy for charge reorganization required upon their heterolytic cleavage is essentially unrecovered at ion-pair transition states.[7] Transition state carbocations for *n*-heptane isomerization to each of its primary products (2-methylhexane and 3-methylhexane) and for secondary isomerization reactions in *n*-heptane isomerization (2-methylhexane to 3-methylhexane and 2,4-dimethylpentane to 2,3-dimethylpentane isomerization) have similar magnitudes and distributions of positive charge and thus interact with conjugate anions with nearly the same electrostatic interaction energies; as a result, transition state energies for these reactions decrease similarly with increases in DPE. The intrinsic (single-sojourn) isomerization selectivities on acids are insensitive to acid strength; they depend, however, on the relative stability of the organic carbocations at the respective ion-pair transition state that mediate the formation of each isomer, which reflects, in turn, the proton affinity of the alkene isomer involved in each skeletal rearrangement.

The isomerization of 2,4-dimethylpentenes involves the same alkyl-substituted carbenium ions as those that mediate *n*-heptene reactions, as well as the interconversion of the primary isomers formed from *n*-heptenes. As a result, the ratio of rate constants for the interconversions among all isomers is also insensitive to acid strength. In the case of *n*-heptene reactants, β-scission occurs at detectable rates only after dimethyl-branched isomers are formed. In contrast, 2,4-dimethylpentenes undergo β-scission and isomerization via parallel direct pathways. The DFT-derived energies for 2,4-dimethylpentane β-scission transition states are less sensitive to DPE than those for 2,4-dimethylpentane isomerization transition states. The ratio of β-scission to isomerization rate constants thus becomes smaller for stronger acids, in contrast with prevalent paradigms that have brought forth contrary claims.[12−15] Measured single-sojourn β-scission to isomerization rate ratios increased exponentially with increasing DPE on MFI zeotypes with different framework heteroatoms; this reflects the more localized charge at the β-scission transition state carbocations compared with isomerization transition states. These species are more "proton-like" and thus recover a larger fraction of the electrostatic component of DPE through more effective Coulombic interactions with the zeotype conjugate anions.

These data and their mechanistic interpretations contradict prevalent paradigms that consider β-scission to become favored over isomerization on stronger acids.[12−15] In fact, weaker acid sites preferentially catalyze β-scission over isomerization as a result of the more effective interaction between conjugate anions and β-scission transition state carbocations. The phenomenological observation that stronger acids favor β-scission merely reflects the greater contribution of diffusion-enhanced secondary reactions on stronger acids, for which more reactive protons favor more severe intracrystalline concentration gradients of product alkenes and greater contributions from diffusion-enhanced secondary β-scission of the primary isomers formed.

2. METHODS AND MATERIALS

2.1. Catalyst Synthesis and Characterization. Heteroatom-substituted MFI zeotypes (Table 1) and mesoporous and microporous aluminosilicates (Table 2; data on Al-MFI samples are listed in both tables) were obtained from commercial sources (BEA, Al-MFI-2: Zeolyst), synthesized using established protocols (FAU, SFH, Al-MFI-1;[8] Fe-MFI, Ga-MFI, B-MFI[6]) or prepared using the procedures described below (SVR, MEL).

Table 1. MFI Zeotype Materials (X-MFI, X = Al, Fe, Ga, B)

solid acid	source	Si/X[a]	H^+/T
Al-MFI-1[b]	ref 8	45.1	0.32[c]
Al-MFI-2[b]	Zeolyst	168	0.62[c]
Ga-MFI	ref 6	109	1.09[d]
Fe-MFI	ref 6	61.1	0.85[d]
B-MFI	ref 6	75.3	0.25[d]

[a] From elemental analysis (ICP-OES; Galbraith Laboratories). [b] Indicated as MFI-1 and MFI-2 in Table 2. [c] From NH_3 evolved during rapid heating of NH_4^+-zeolites.[8] [d] From titration with pyridine during methanol dehydration reactions.[6]

DOI: 10.1021/acs.jpcc.8b08460
J. Phys. Chem. C 2018, 122, 25475−25497

Table 2. Mesoporous and Microporous Aluminosilicate Materials

solid acid	source	Si/Al[a]	H^+/Al
Al-MCM-41	Sigma-Aldrich	37.8	0.36[b]
FAU	ref 8	7.5	0.39[b]
SFH	ref 8	45.0	0.71[b]
MEL	section 2.1	20.6	0.75[c]
BEA	Zeolyst	43.3	0.37[c]
SVR	section 2.1	20.2	0.20[c]
MFI-1[d]	ref 8	45.1	0.32[c]
MFI-2[d]	Zeolyst	168	0.62[c]
(Na)MFI-2[e]	section 2.1	168	0.02[f]

[a] From elemental analysis (ICP-OES; Galbraith Laboratories). [b] From titration with 2,6-di-*tert*-butylpyridine during *n*-heptane isomerization reactions.[8] [c] From NH_3 evolved during rapid heating of NH_4^+-zeolites.[8] [d] Indicated as Al-MFI-1 and Al-MFI-2 in Table 1. [e] Na-exchanged form of MFI-2 (Section 2.1). [f] By difference from Na contents.

SVR was prepared by mixing NaOH (EMD Chemicals, 0.80 g), $Al(OH)_3$ (53% Al_2O_3, Reheis F-2000 dried gel, 0.96 g), and hexamethylene-1,6-bis(*N*-methyl-*N*-pyrrolidinium) hydroxide (synthesized using reported protocols,[18] 0.73 mM, 27.4 g). SVR seeds (0.60 g) and amorphous SiO_2 (96% SiO_2, CAB-O-SIL M5, 12.4 g) were then added and mixed thoroughly with a spatula. The mixture was kept at ambient conditions and then ground with a mortar and pestle. The resulting powders were placed within a Teflon liner held in an autoclave (Parr, 150 cm^3; static) at 423 K for 28 days.

MEL was prepared by mixing *N*,*N*-diethyl-3,5-dimethylpiperidinium hydroxide (synthesized as reported previously,[19] 2.25 mmol) in deionized water (4 g) and then adding NaOH (EMD Chemicals, 1M, 1.5 mmol) and $Al(OH)_3$ (53% Al_2O_3, Reheis F-2000 dried gel, 0.066 g). Once the suspension was clear, amorphous SiO_2 (96% SiO_2, Cab-O-Sil M5, 0.90 g) and MEL seeds (3 wt %) were added; the mixtures were held within a Teflon-lined autoclave (Parr, 23 cm^3; 43/60 Hz) at 433 K for 8 days. The solids were collected by filtration, washed with deionized water (until the filtrate conductivity was <50 S/m), and then treated under dynamic vacuum at ambient temperature for 12 h.

All samples were treated in dry air (2.5 $cm^3\ g^{-1}\ s^{-1}$, extra dry, Praxair) at 823 K (0.0167 K s^{-1}) for 4 h. Aluminosilicate samples were converted to their NH_4^+ forms by contacting them with aqueous 0.1 M NH_4NO_3 (>98%, Sigma-Aldrich; 300 g solution [g zeolite]$^{-1}$).[8] The pH of the NH_4NO_3 solutions (5−6) can lead to the extraction of some of the Fe^{3+} and B^{3+} heteroatoms from their tetrahedral framework locations;[20] as a result, Fe-MFI, Ga-MFI, and B-MFI samples were NH_4^+-exchanged using an aqueous 0.1 M $NH_4C_2H_3O_2$ solution of neutral pH (>99%, Sigma-Aldrich; ~300 g of solution [g zeotype]$^{-1}$; pH ~7).

MFI-2 was prepared in its Na form ((Na)MFI-2, Table 2) by exchange of MFI-2 with 1.0 M $NaNO_3$ (>98%, EMD Millipore; ~300 g of solution [g zeolite]$^{-1}$) at 353 K for 12 h. All solids were separated using vacuum filtration, rinsed with deionized water (resistivity >17.6 Ω cm^{-2}; ~1500 g [g zeolite]$^{-1}$), and treated under dynamic vacuum at ambient temperatures for 12 h. The concentrations of Si, Al, Ga, Fe, B, and Na in each sample were measured by inductively coupled plasma optical emission spectroscopy (ICP-OES; Galbraith Laboratories).

The number of protons in each aluminosilicate or zeotype was determined by one of three methods: (i) titration with selective titrant 2,6-di-*tert*-butylpyridine (DTBP; assuming 1:1 DTBP:H^+ stoichiometry) during *n*-heptane isomerization[8] (Al-MCM-41, FAU); (ii) titration with pyridine (assuming 1:1 pyridine:H^+ stoichiometry) during methanol dehydration[6] (Fe-MFI, Ga-MFI, B-MFI); or (iii) evolution of NH_3 (assuming 1:1 NH_3:H^+ stoichiometry) during thermal treatment of NH_4^+-exchanged zeolites[8] (SFH, BEA, MEL, Al-MFI, SVR). The number of protons in (Na)MFI-2 was determined by difference from its Na content. DTBP titrants selectively interact with Brønsted acid sites because their bulky *t*-butyl substituents prevent coordination to Lewis acid centers;[21] isomerization rates are fully suppressed during *n*-heptane isomerization on Al-MCM-41 and FAU[8] at DTBP uptakes smaller than the Al contents of the samples (0.36 and 0.39 DTBP/Al, respectively), indicating that Lewis acid sites, present as extraframework Al species, do not catalyze isomerization at these conditions. DTBP titrants, however, cannot diffuse into medium-pore zeolites (MEL, MFI, SVR) or one-dimensional large-pore zeolites (SFH). Smaller pyridine titrants introduced during methanol dehydration reactions at 433 K can diffuse into MFI and interact with both Brønsted and Lewis acid sites but bind irreversibly only to protons at these conditions,[6] thus allowing accurate proton counts for medium-pore materials (Ga-, Fe-, B-MFI). These titrants are not suitable for use during alkane isomerization on bifunctional catalysts because they convert to other species via reactions with H_2 on the metal function. Proton counts were measured on the other materials (Al-MFI, MEL, SVR, and SFH) from the amount of NH_3 evolved during rapid heating of their respective NH_4^+-exchanged forms. As described in previous work,[8] this specific BEA material contains protons located in two distinct confining environments, the result of stacking faults and polymorph intergrowths prevalent in BEA-framework materials and reflected in two distinct peaks (~673 K and ~898 K) in the NH_3 evolution profile; protons associated with the lower-temperature NH_3 evolution peak (~673 K) were used to estimate the number of protons accessible to reactants in these samples.

Pt/SiO_2 was prepared and treated as described previously.[8] The Pt dispersion (88%; corresponding to particles ~1 nm in diameter) was determined from total H_2 uptakes at 373 K using a 1:1 H:Pt_s stoichiometry (Pt_s is the number of surface Pt atoms). Intimate physical mixtures of Pt/SiO_2 with each aluminosilicate or zeotype were prepared by combining the two powders (crushed and sieved to <125 μm before mixing), pressing into pellets (Carver Bench Top Manual Press, <8000 psi), and crushing and sieving to retain aggregates 180−250 μm in size. The metal function in each mixture is reported as its Pt_s/H^+ ratio, using the Pt_s from chemisorption uptakes and the proton densities reported in Tables 1 and 2 for each sample. The Pt_s/H^+ ratios used in all catalytic experiments were sufficient to equilibrate alkane reactants with their respective alkenes (Pt_s/H^+ >7.8) within the interstices between zeolite crystals. These ratios were found to equilibrate *n*-heptane/heptenes-H_2 during *n*-heptane isomerization on bifunctional catalysts.[8] 2,4-Dimethylpentane consumption rates were more than 5-fold lower than *n*-heptane isomerization turnover rates on MFI-1 and MFI-2; consequently, such Pt_s/H^+ ratios are deemed to be sufficient to provide equilibrium concentrations of all 2,4-dimethylpentene isomers in the extracrystalline fluid phase. All mixtures are denoted by the identity of their acid function (Tables 1 and 2; e.g., B-MFI for physical mixtures of Pt/SiO_2 and B-MFI).

2.2. 2,4-Dimethylpentane and *n*-Heptane Isomerization and *β*-Scission Rate and Selectivity Measure-

DOI: 10.1021/acs.jpcc.8b08460
J. Phys. Chem. C 2018, 122, 25475−25497

ments. Turnover rates for isomerization and β-scission reactions of 2,4-dimethylpentane (24DMP) and *n*-heptane (nC_7) were measured at 548 K on all samples (0.050−0.150 g) using a tubular reactor (316 S.S., 12 mm i.d.) with plug-flow hydrodynamics at differential reactant conversions (<10%). Temperatures were measured using a K-type thermocouple held within an axial thermowell at the center of the catalyst bed; temperatures were kept constant using a three-zone resistively heated furnace (Applied Test Systems Series 3210) and three independent electronic controllers (Watlow, EZ-ZONE PM Series). Samples were treated in a 10% H_2/He mixture (0.83 cm^3 s^{-1}; 99.999% Praxair H_2; 99.999% Praxair He) at 573 K (0.083 K s^{-1}) for 2 h before cooling to reaction temperatures. *n*-Heptane (>99.5%, Acros Organics; used as received) and 2,4-dimethylpentane (99%, Sigma-Aldrich; used as received) were introduced in their liquid form into flowing H_2 (99.999%, Praxair) and He (99.999%, Praxair) mixed streams using a syringe pump (Cole-Parmer 780200C series). Alkane and H_2 concentrations were varied independently (60−100 kPa H_2; H_2/alkane = 2.5−300) through changes in the gas and liquid flow rates. All transfer lines after liquid introduction were heated above 423 K to prevent condensation. Reactant and product concentrations in the effluent stream were measured using online gas chromatography (Agilent 6890N GC) by separating species with a methyl silicone capillary column (Agilent HP-1; 50 m × 0.32 mm × 1.05 μm) and measuring their concentrations using a flame ionization detector. The concentrations of trace impurities of product alkanes in reactant 24DMP (0.2 mol % 2,3-dimethylpentane, 2-methylhexane, and 3-methylhexane) were subtracted from those measured in the reactor effluent in all rate calculations.

Rates are reported here as turnover rates using measured molar conversion rates normalized by the number of H^+ in each sample (Tables 1 and 2). All reported uncertainties denote 95% confidence intervals. Turnover rates were corrected for approach to equilibrium ($\eta_{j,i}$) for the conversion of each reactant (react) to each isomer or β-scission product (prod)

$$r_{\text{forward}} = r_{\text{net}}(1 - \eta_{\text{prod,react}})^{-1} \tag{1}$$

The approach to equilibrium ($\eta_{j,i}$) for the monomolecular isomerization reaction that converts species i to species j is defined as

$$\eta_{j,i} = \left(\frac{P_j}{P_i}\right)K_{j,i}^{-1} \tag{2}$$

P_j and P_i are the pressures (in bar) of species j and species i, respectively, and $K_{j,i}$ is the equilibrium constant calculated at 548 K from tabulated thermodynamic data[22] for each i−j pair. The approach to equilibrium for β-scission of the species i ($\eta_{\beta,i}$) is defined as

$$\eta_{\beta,i} = \left(\frac{P_{C_3}P_{C_4}}{P_i}\right)K_{\beta,i}^{-1} \tag{3}$$

P_{C_3} and P_{C_4} are the pressures (in bar) of C_3 and C_4 β-scission products, respectively, and $K_{\beta,i}$ is the equilibrium constant for β-scission reactions of species i at 548 K, obtained from tabulated thermodynamic data.[22] Measured β-scission products remained far from equilibrium at all conditions ($\eta_{\beta,nC7}$ and $\eta_{\beta,24DMP}$ $<10^{-4}$), thus rendering any corrections unnecessary.

Rates were measured periodically at reference conditions (100 kPa H_2, 0.5 kPa alkane) to correct for any intervening deactivation. Deactivation was nearly undetectable for *n*-heptane reactants (<5% change after 60 h) but became more significant for 2,4-dimethylpentane, especially at low H_2/alkane ratios (~20% rate decrease after 4 h).

Fractional selectivities ($S_{\text{react,prod}}$) are reported on a C atom basis

$$S_{\text{react,prod}} = \frac{r_{\text{react,prod}}}{\sum_{\text{prod}} r_{\text{react,prod}}} \tag{4}$$

where $r_{\text{react,prod}}$ is the measured formation rate of each product (prod; in terms of moles of reactants consumed) from each reactant (react). These fractional selectivities are distinct from single-sojourn selectivities (eq 5) because secondary reactions of alkene products that occur during their egress from the acid domain result in selectivities that do not reflect single-sojourn events.

The product selectivities for 24DMP and nC_7 reactants were measured as the number of accessible protons increased monotonically with time during the desorption of preadsorbed NH_3 titrants, which bind reversibly at reaction temperatures (548 K). Samples treated as described above were used for rate measurements (100 kPa H_2; H_2/alkane ~200) and then exposed to a stream containing 0.5 kPa NH_3 (0.83 cm^3 s^{-1}, 1% NH_3 in He, Praxair; diluted with He, 99.999%, Praxair) for 2 h. These titrated samples were exposed to the reactant stream (100 kPa H_2; H_2/alkane ~200); rates and selectivities (eq 4) were measured as the NH_3 titrants gradually desorbed, and reaction rates concurrently increased as protons became accessible for catalytic turnovers. Rates returned to 70−90% of their initial values after 2 h, as a result of some intervening deactivation during these measurements.

Fractional selectivities extrapolated to zero proton densities during NH_3 desorption (for zeolites) or to zero residence time (for Al-MCM-41) ($S_{\text{react,prod,0}}$) are defined as

$$S_{\text{react,prod,0}} = \frac{r_{\text{react,prod,0}}}{\sum_{\text{prod}} r_{\text{react,prod,0}}} \tag{5}$$

where the subscript "0" denotes product formation rates resulting from single sojourns at active sites. These values reflect intrinsic selectivities for mesoporous and large-pore aluminosilicates but not for medium-pore zeolites, as discussed in Section 3.2 below, as a result of local undulations in their void environment that permit product readsorption and secondary reactions even at a single proton.

The fraction of steady-state rates measured at each time during NH_3 desorption ($\chi(t)$) is defined as

$$\chi(t) = \frac{r_{\text{react}}(t)}{r_{\text{react}}} \tag{6}$$

The $r_{\text{react}}(t)$ term is the rate at each time during NH_3 desorption, and r_{react} is the steady-state reaction rate measured before each sample was exposed to NH_3. The effects of intracrystalline proton densities, varied systematically as NH_3 desorbs, are used to interpret the effects of diffusion-enhanced secondary reactions on selectivities, as described in Section 3.2 and as implemented in a previous study of *n*-heptane isomerization and β-scission reactions.[8]

2.3. Density Functional Theory Methods. The energies and structures of transition states and reactants involved in linear heptene and 2,4-dimethylpentene isomerization and β-scission in MFI zeotypes were calculated using periodic plane-wave density functional theory (DFT) as implemented in the Vienna *ab initio* simulation package (VASP)[23−26] using a plane-wave energy cutoff of 396 eV, projector-augmented wave potentials (PAW),[27,28] the revised Perdew−Burke−Ernzerhof (RPBE) functional,[29,30] and semiempirical DFT-D3 with Becke−Johnson (BJ) damping[31,32] (to account for dispersive interactions). A (1 × 1 × 1) Γ-centered k-point mesh was used to sample the first Brillouin zone. Structures were relaxed until electronic energies varied by $<1 \times 10^{-6}$ eV, and forces on all atoms were <0.05 eV Å^{-1}. Transition state energies and structures for heptene and 2,4-dimethylpentene isomerization and β-scission reactions on MFI zeotypes were obtained by calculating minimum energy paths using the nudged elastic band (NEB) method;[33] individual structures along the NEB were converged to $<1 \times 10^{-4}$ eV (energy) and total forces on atoms <0.3 eV Å^{-1}. Structures were subsequently refined using Henkelman's dimer method,[34] converged to $<1 \times 10^{-6}$ eV for energy and <0.05 eV Å^{-1} for forces. Löwdin population analyses[35] were used to obtain charge distributions for converged structures after transforming wave functions into localized quasi-atomic orbitals (QUAMBO).[36−39]

MFI zeotype structures were constructed with one heteroatom per unit cell (Si/T = 95) using the numbering convention of Olson[40] to denote specific framework atoms within the unit cell. Unit cells were initially constructed in the siliceous form, using orthorhombic unit cell parameters (2.0022 nm × 1.9899 nm × 1.3383 nm, $\alpha = \beta = \gamma = 90°$; used without further geometric relaxation) and atom coordinates determined from X-ray diffraction.[41] The Si-12 framework site was isomorphously substituted with Al^{3+}, Ga^{3+}, Fe^{3+}, or B^{3+}, and the requisite charge-balancing proton was placed at O-20 for each zeotype structure. Transition state structures and energies were obtained for Brønsted acid sites only at this location, which lies at the intersection of the straight and sinusoidal channels in MFI; Figure 1 shows the location of the T-12 and the optimized structure of a 2,4-dimethylpentene isomerization transition state for an Al residing at that location (Figure 1a shows a view along the straight channel and Figure 1b along the sinusoidal channel).

DPE values cannot be accurately determined using periodic DFT methods because of charged defects[42] that result in artificially high DPE values (by ∼400 kJ mol^{-1} for Al-MFI[16]); DPE values previously determined using cluster methods and larger MFI clusters are instead used here.[7]

Energy barriers for the formation of transition states ($E_{\text{app,react,prod}}$ for the transition state to form product (prod) from reactant (react)) from relevant precursors were calculated from

$$E_{\text{app,react,prod}} = E_{\text{react,prod}}{}^{\ddagger} - \sum_{\text{ref}} E^{\text{ref}} \tag{7}$$

where $E^{\ddagger}_{\text{react,prod}}$ is the transition state energy and E^{ref} are the energies of the reference states appropriate for each calculation. Isomerization events occur through several different transition states that mediate the conversion of a given reactant alkene, through specific reactant alkoxides, into a particular product alkoxide with a different skeletal backbone.[8] The energies of all of these transition states contribute to measured rates for the formation of that skeletal isomer; all of these energies are taken into account here in determining the energy of such a transition state ensemble ($\langle E^{\ddagger}_{\text{react,prod}} \rangle$) using

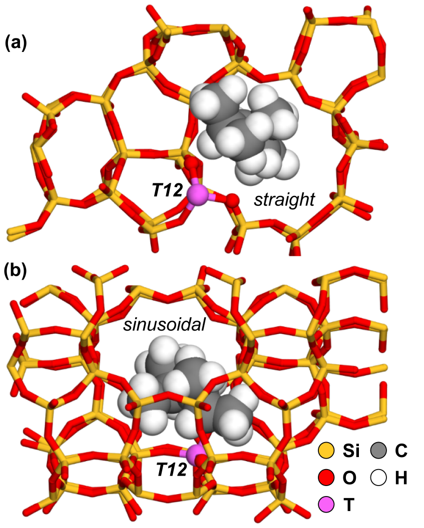

Figure 1. 2,4-Dimethylpent-2-ene isomerization (to 2,3-dimethylpent-4-ene) transition state converged at the T12-O20(H) site in MFI (VASP, RPBE + D3(BJ)). Framework Si and O atoms are yellow and red, respectively; the magenta atom denotes the T12 site. The transition state carbocation is represented using a space-filling model; gray atoms are carbon, and white atoms are hydrogen. (a) is a view along the straight channel of MFI, with part of the structure excised for visual clarity after structural optimization. (b) is a view along the sinusoidal channel.

$$\langle E_{\text{react,prod}}{}^{\ddagger} \rangle = -k_B T \ln\left(\sum_n \exp\left(\frac{-E_{\text{react,prod,n}}{}^{\ddagger}}{k_B T}\right)\right) \tag{8}$$

Here, k_B is the Boltzmann constant; T is temperature; and $E^{\ddagger}_{\text{react,prod},n}$ is the energy of each specific transition state n.

Acid strength effects are determined by examining one specific transition state among all the transition states converting a specific alkene (through its various alkoxide regioisomers) to an alkene with a different skeletal backbone. Multiple transition state configurations (>20) were first calculated for each reaction pathway; the specific transition state examined was chosen for having the lowest energy among all transition state configurations because its low energy results in its contributing most significantly to the energy of the transition state ensemble (eq 8).

3. RESULTS AND DISCUSSION

n-Heptane (nC_7) and 2,4-dimethylpentane (24DMP) isomerization and β-scission rates and selectivities were measured on MFI zeotypes with different heteroatoms (X-MFI, where X = Al, Ga, Fe, B; Table 1). These zeotypes contain sites of very different acid strengths but which are located within a similar confining framework. 24DMP consumption rates and selectivities were also measured on mesoporous and microporous aluminosilicates (Al-MCM-41, FAU, SFH, MEL, BEA, SVR; Table 2); these solids contain sites that are similar in acid strength[16,17] but reside within very diverse confining void environments. All solid acid catalysts were used as intimate physical mixtures with Pt/SiO_2. Reaction rates measured on such bifunctional mixtures were >100-fold larger than on either of the two monofunctional components consistent with alkane isomerization and β-scission routes that require unsaturated species formed at the metal function and their kinetically relevant skeletal rearrangement or C−C bond cleavage on acid sites.

A rigorous assessment of the effects of acid strength on reactivity and selectivity requires that all acid sites exist in contact with the (known) extracrystalline concentrations of reactant-derived alkenes. This requires, in turn, that alkane reactants equilibrate with all their alkene regioisomers at the extracrystalline Pt function. It also requires that these equilibrium concentrations persist throughout the metal-free acid domains without any gradients caused by either slow diffusion or fast reactions. Mixtures with Pt_s/H^+ ratios above 8 (Pt_s is the number of Pt surface atoms from H_2 chemisorption and H^+ are the proton counts reported in Tables 1 and 2) gave similar rates at 548 K, indicating that such Pt contents are sufficient to establish hydrogenation−dehydrogenation equilibrium within the extracrystalline fluid phase for nC_7 reactions on Al-MFI.[8] Measured turnover rates for nC_7 isomerization on MFI are more than 5-fold larger than for 24DMP on all acids, while equilibration of 24DMP and nC_7 hydrogenation−dehydrogenation is likely to occur at similar rates (and possibly even faster for branched isomers with weaker C−H bonds).[43] Thus, similar Pt_s/H^+ ratios are sufficient for the equilibration of 24DMP and nC_7 with their respective alkene regiosomers on these physical mixtures.

nC_7 isomerization rates on these aluminosilicates were previously shown[8] to be unaffected by gradients in reactant alkene concentrations from the similar rates measured on MFI samples with different proton density and crystal size. The presence and severity of alkene concentration gradients within zeolite and zeotype crystallites for 24DMP reactants are discussed in the SI (section S6).

3.1. Elementary Steps That Mediate *n*-Heptane Turnovers and Acid Strength Effects on Isomerization Turnover Rates and Selectivity. In this section, we report *n*-heptane isomerization turnover rates and address the catalytic consequences of acid strength in the context of the sequence of elementary steps that mediate such reactions. Figure 2 shows *n*-heptane (nC_7) isomerization rates (per H^+) on physical mixtures of MFI zeotypes of different acid strength and Pt/SiO_2; these rates are denoted as isomerization rates because 2-methylhexenes and 3-methylhexenes are the only products formed directly from *n*-heptenes in a single sojourn at protons on these catalysts.[8] All 2-methylhexene and 3-methylhexene regioisomers equilibrate through facile methyl shifts and are treated here as equilibrated methylhexene lumped chemical species. These methylhexenes then form dimethylpentenes, with 2,4-dimethylpentene skeletal isomers as the predominant precursors to *β*-scission products, as shown by DFT-derived transition state free energies for *β*-scission from all skeletal isomers.[8] This reaction network for *n*-heptane isomerization and *β*-scission is depicted in Scheme 1a using the saturated analogues of reactive alkenes for visual clarity and simplicity.

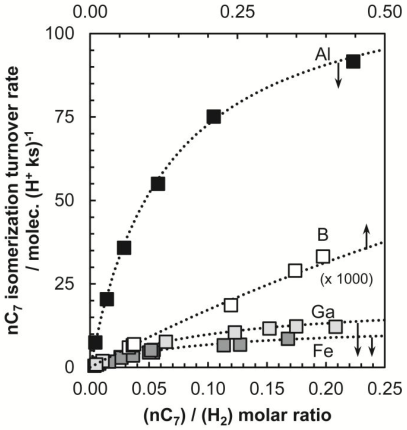

Figure 2. *n*-Heptane isomerization turnover rates as a function of $(nC_7)/(H_2)$ molar ratio on physical mixtures of Pt/SiO_2 and X-MFI (X = Al, Ga, Fe, B) (548 K, 60−100 kPa H_2). Dashed curves represent regression to eq 10.

n-Heptane isomerization turnover rates (Figure 2; per H^+) depend linearly on nC_7/H_2 reactant ratios at low ratios but approach constant rates at higher molar ratios. Measured rates are accurately described (Figure 2, dashed curves) by

$$\frac{r_{\mathrm{isom,nC_7}}}{[\mathrm{H^+}]} = \frac{k_{\mathrm{first}}(\mathrm{nC_7/H_2})}{1 + k_{\mathrm{first}}/k_{\mathrm{zero}}(\mathrm{nC_7/H_2})} \tag{9}$$

in which k_{first} and k_{zero} represent the first-order and zero-order kinetic parameters, defined, in turn, by the kinetic and thermodynamic constants for the required elementary steps in Scheme 2a. The functional form of eq 9 is consistent with the sequence in Scheme 2a, wherein the steps are illustrated for nC_7 isomerization to 2-methylhexane (2MH), occurring through one specific heptoxide attachment isomer and forming a specific 2-methylhexoxide attachment isomer. These steps consist of: (1) *n*-heptane dehydrogenation to equilibrated linear heptenes (Scheme 2a, Step 1: *n*-heptane to 2-heptene); (2) quasi-equilibrated protonation of these heptenes to form all different heptoxide attachment isomers (defined by the C atom bound to the framework O atom (Scheme 2a, Step 2: 2-heptene to hept-3-oxide); (3) skeletal isomerization of these heptoxides to all attachment isomers of 2-methylhexoxides and 3-methylhexoxides in the sole kinetically relevant step (Scheme 2a, Step 3: hept-3-oxide to 2-methylhex-1-oxide); (4) quasi-equilibrated *β*-hydrogen elimination to form 2-methylhexenes and 3-methylhexenes (Scheme 2a, Step 4: 2-methylhex-1-oxide to 2-methylhex-1-ene); and (5) equilibrated hydrogenation of alkene products to their respective (less reactive) alkanes (Scheme 2a, Step 5: 2-methylhex-1-ene to 2-methylhexane) on the extracrystalline metal function. Steps (1) and (5) occur on the metal function, while Steps (2)−(4) occur at acid sites. This sequence, taken together with bare protons and reactant-derived heptoxides as the most abundant surface intermediates (MASI), leads to the functional form of eq 9.

Scheme 2a depicts the specific transformations that converts hept-3-oxides to 2-methylhex-1-oxides as an illustrative example. Measured *n*-heptane isomerization rates, however, reflect the combined contributions of skeletal isomerization events of all heptoxide attachment isomers through all the transition states that form each of the 2-methylhexoxide and 3-methylhexoxide attachment isomers, as discussed previously[8] and in Section 2.3; each pathway can be described by elementary steps analogous to those in Scheme 2a. The summation of the rate expressions for each pathway gives an equation with effective kinetic and thermodynamic parameters (shown explicitly as the summation of rate expressions in the SI, section S1):

$$\frac{r_{\mathrm{isom},nC_7}}{[\mathrm{H^+}]} = \frac{k_{\mathrm{isom},nC_7} K_{\mathrm{prot},nC_7} K_{\mathrm{dehyd},nC_7} (nC_7/\mathrm{H_2})}{1 + K_{\mathrm{prot},nC_7} K_{\mathrm{dehyd},nC_7} (nC_7/\mathrm{H_2})} \tag{10}$$

Scheme 1. Reaction Network for (a) *n*-Heptane and (b) 2,4-Dimethylpentane Isomerization and *β*-Scission on Physical Mixtures of Pt/SiO$_2$ and Solid Brønsted Acids, Represented by the Saturated Analogues of the Reactive Alkene Species[a]

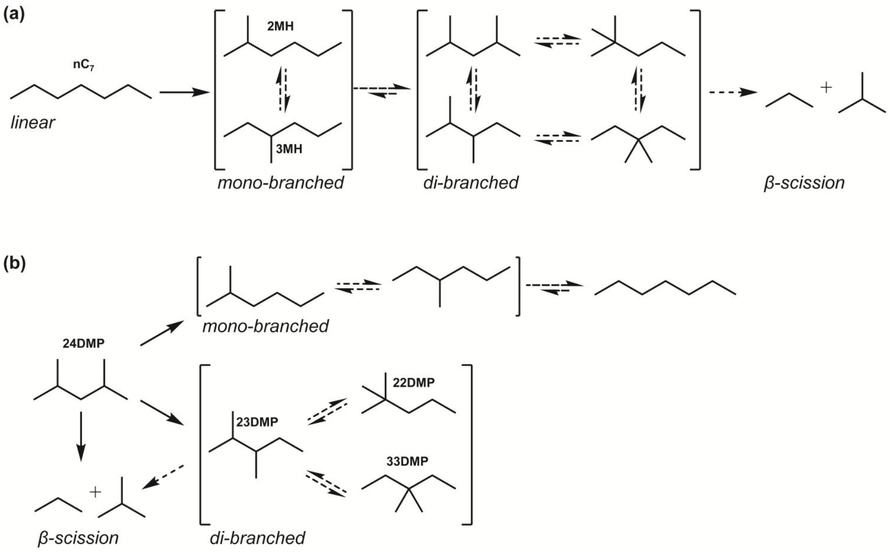

[a] Black arrows indicate primary reactions, and dashed arrows indicate secondary reactions. Brackets around isomers with the same degree of branching indicate facile interconversion and isomers present as equilibrated mixtures.

The effective constants are given by (i) k_{isom,nC_7}, the rate constant for skeletal isomerization of heptoxides to equilibrated methylhexoxide products; (ii) K_{prot,nC_7}, the equilibrium constant for the formation of heptoxides from linear heptenes; and (iii) K_{dehyd,nC_7}, the equilibrium constant for nC$_7$ dehydrogenation to an equilibrated mixture of all linear heptene regioisomers.

Scheme 3 shows the reaction coordinate diagram for nC$_7$ isomerization reactions, denoting ensemble free energies ($\langle G^m \rangle$, for ensemble m with n distinct configurations) for heptoxides ($\langle G^{nC_7*} \rangle$) and for heptoxide-derived transition states ($\langle G^{nC_7\ddagger} \rangle$). These ensemble free energies are defined by

$$\langle G^m \rangle = -k_B T \ln\left(\sum_n \exp\left(\frac{-G_n^m}{k_B T}\right)\right) \tag{11}$$

where T is temperature and k_B is the Boltzmann constant. The first-order rate constants ($k_{\mathrm{isom},nC_7}K_{\mathrm{prot},nC_7}K_{\mathrm{dehyd},nC_7}$ in eq 10) reflect the free energy differences for the ensemble of transition states ($\langle \Delta G^{\ddagger}_{\mathrm{app},nC_7} \rangle$)

$$k_{\mathrm{isom},nC_7}K_{\mathrm{prot},nC_7}K_{\mathrm{dehyd},nC_7} = \frac{k_B T}{h}\exp\left(\frac{-\langle \Delta G^{\ddagger}_{\mathrm{app},nC_7} \rangle}{k_B T}\right)$$

$$\frac{k_B T}{h}\exp\left(-\frac{\langle G^{nC_7\ddagger} \rangle - G^{nC_7(g)} + G^{H_2(g)} - G^{H^+}}{k_B T}\right) \tag{12}$$

G^{H+}, $G^{nC_7(g)}$, $G^{H_2(g)}$, and $\langle G^{nC_7\ddagger} \rangle$ denote the free energies of bare protons, gaseous nC$_7$, gaseous H$_2$, and the ensemble of all ion-pair transition states that form all 2-methylhexoxide and 3-methylhexoxide attachment isomers from all possible heptoxide attachment isomers; h is Planck's constant. Reactant alkenes and their respective alkoxides are each assumed to be equilibrated chemical species in these kinetic treatments and denoted with superscript "=" and "*", respectively (e.g., nC$_7^=$, nC$_7$*, 24DMP$^=$, 24DMP*); specific regioisomers contained within each equilibrated group are shown in Scheme 3 using nC$_7^=$ and nC$_7$* as illustrative examples.

The first-order ($k_{\mathrm{isom},nC_7}K_{\mathrm{prot},nC_7}K_{\mathrm{dehyd},nC_7}$) and zero-order ($k_{\mathrm{isom},nC_7}$) rate constants were determined by regressing all rate data to the form of eq 10. Table 3 shows that $k_{\mathrm{isom},nC_7}K_{\mathrm{prot},nC_7}K_{\mathrm{dehyd},nC_7}$ values for MFI zeotypes vary by about 10^4-fold among samples with different framework heteroatoms. The values of the zero-order rate constants are included in the SI (section S2); their uncertainties are much greater than for first-order rate constants because K_{prot,nC_7} becomes measurable only as alkoxide coverages increase with alkene pressure. Such coverages lead to detectable oligomerization and deactivation events, which must be accounted for in isolating the kinetic effects of alkene pressure from the concomitant effects of deactivation on the density of remaining acid sites.

The rigorous interpretation of acid strength effects on reactivity requires rate constants (per H$^+$) to be of strict kinetic origin. Such a requirement was shown to be fulfilled for $k_{\mathrm{isom},nC_7}K_{\mathrm{prot},nC_7}K_{\mathrm{dehyd},nC_7}$ values on Al-MFI in previous work from nC$_7$ isomerization turnover rates on samples with different Thiele moduli (ϕ_i for molecule i; discussed in the SI (section S6) for 24DMP reactants)[8]

$$\phi_i^2 = \frac{\alpha_i \rho_{H^+} R^2}{D_i} \tag{13}$$

where α_i and D_i are the first-order rate constant and the molecular diffusivity of molecule i; R is crystallite radius; and ρ_{H^+} is intracrystalline proton density. The Thiele modulus (eq 13) is derived from a reaction-transport analysis,[44,45] and it is the sole descriptor of the severity of intracrystalline concentration gradients. Small ϕ_i values ($\leq$1) are indicative of the strict chemical origins of measured turnover rates, while large ϕ_i values (>1) reflect the onset of intracrystalline concentration gradients of reactant alkenes. The ratio of the measured and intrinsic kinetic rate constants ($k_{\mathrm{first,i,meas}}$ and $k_{\mathrm{first},i}$, respectively; Γ_i, the effectiveness factor) then depends on on ϕ_i[44,45]

Scheme 2. Elementary Steps in (a) *n*-Heptane Isomerization to 2-Methylhexane and (b) 2,4-Dimethylpentane Isomerization to 2,3-Dimethylpentane and *β*-Scission to Isobutane and Propane on Physical Mixtures of Solid Brønsted Acids and Pt/SiO_2[a]

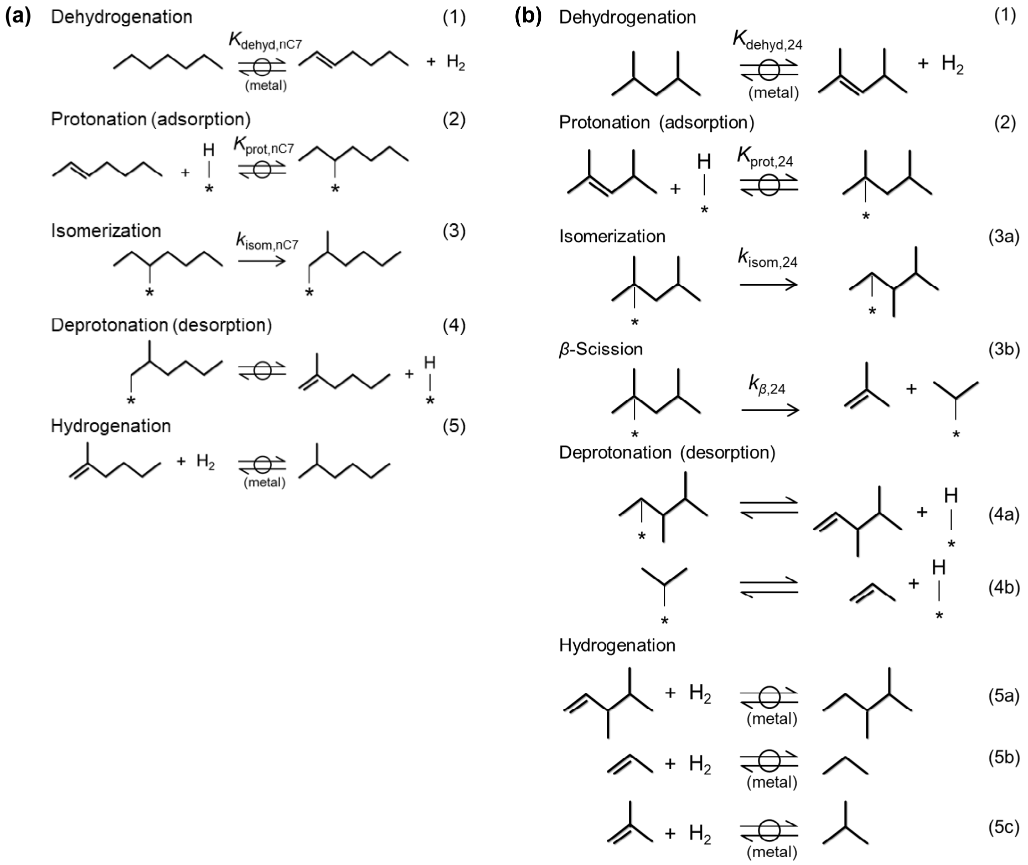

[a]Alkane dehydrogenation (Steps 1) and alkene hydrogenation steps (Steps 5) are quasi-equilibrated on Pt/SiO_2 (the metal function). Steps 2–4 occur on acid sites. Steps 3a, 4a, and 5a represent the formation of alkene isomer products with the 2,3-dimethylpentane skeletal structure; analogous steps also form products with the 2-methylhexane backbone. Attachment points of protons and alkoxides to inorganic framework structures are indicated by the symbol "*" in the molecular structures. Double-bond regioisomers and surface alkoxides with a given backbone are equilibrated; those included in the scheme were chosen for illustrative purposes.

$$\Gamma_i \equiv \frac{k_{\text{first},i,\text{meas}}}{k_{\text{first},i}} = \frac{3}{\phi_i^2}(\phi_i \coth(\phi_i) - 1) \tag{14}$$

for quasi-spherical crystallites. We note that the typical nomenclature for the effectiveness factor is the Greek symbol η, which has been used in this work to indicate approach to equilibrium values.

The presence and severity of such concentration gradients within MFI-zeotype crystallites can be rigorously assessed from the magnitude of $\phi_{nC_7^=}$ (eq 13). $D_{nC_7^=}$ at reaction conditions cannot be measured because alkenes would react as such conditions on zeolitic protons. Their values, however, are expected to be similar for MFI frameworks with different heteroatoms. Values of $\alpha_{nC_7^=}R^2\rho_{H^+}$ therefore represent an accurate simplification of $\phi_{nC_7^=}$ (eq 13) for zeotypes with a given framework structure. The values of the $\alpha_{nC_7^=}R^2\rho_{H^+}$ for Al-MFI-1 and Al-MFI-2 were smaller (by factors of 100 and 10, respectively) than for the Al-MFI sample for which the reactant $nC_7^=$ concentration gradients were kinetically relevant.[8] The H^+ densities in Ga, Fe, and B-MFI samples are similar to (or smaller than) those in Al-MFI (Table 2), and their nC_7 isomerization rate constants ($k_{\text{isom},nC_7}K_{\text{prot},nC_7}K_{\text{dehyd},nC_7}$; Table 3) are more than 10-fold smaller than on Al-MFI. These considerations, along with crystallite sizes (~50–100 nm; estimated from microscopy, section S3, SI), preclude concentration gradients of reactant alkenes within any of these MFI zeotypes. Measured first-order rate constants for nC_7 isomerization on X-MFI (X = Al, Ga, Fe, B) therefore reflect their true chemical origins; their sensitivity to acid strength can be mechanistically interpreted, as discussed next.

The stability of the ion-pair transition states that mediate the different pathways for *n*-heptane isomerization routes depends on the stability of the conjugate anion and thus on acid strength, as evident from the strong effects of deprotonation energy (DPE) on $k_{\text{isom},nC_7}K_{\text{prot},nC_7}K_{\text{dehyd},nC_7}$ for MFI zeotypes (X-MFI, where X = Al, Ga, Fe, B; DPE = 1167–1214 kJ mol^{-1}) (Figure 3). These zeotypes contain acid sites that reside within confining voids of the same size and shape but with conjugate anions that differ significantly in stability. Measured first-order rate constants ($k_{\text{isom},nC_7}K_{\text{prot},nC_7}K_{\text{dehyd},nC_7}$ values) decrease exponentially with increasing DPE (Figure 3), the rigorous metric of the stability of the conjugate anion and the rigorous descriptor of acid strength. These effects of DPE on rate constants predominantly reflect changes in activation barriers ($\langle E_{\text{app},nC_7}\rangle$ for nC_7 isomerization) instead of changes in activation

Scheme 3. Reaction Coordinate Diagram with the Free Energies That Determine the Rate Constants (per H^+) for *n*-Heptane Isomerization Reactions[a]

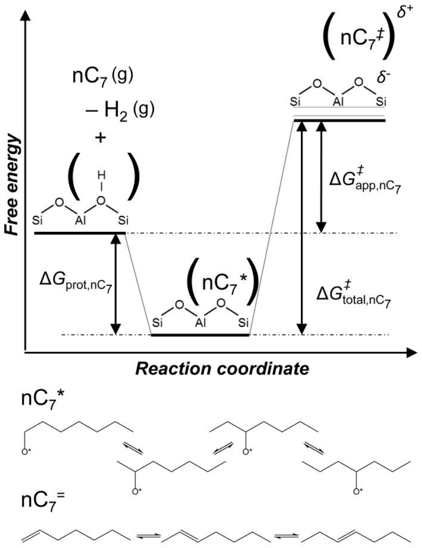

[a]Equilibrated species denoted as $nC_7^=$ (alkene regioisomers) and nC_7^* (alkoxides of different attachment points) are indicated in the space below the coordinate. Grey lines below the transition state indicate free energies of specific transition state configurations (i.e., isomerization), while the dark black line indicates the free energy of the transition state ensemble of all individual configurations.

Table 3. First-Order Rate Constants (per H^+, 548 K) for nC_7 Isomerization ($k_{\mathrm{isom},nC_7}K_{\mathrm{prot},nC_7}K_{\mathrm{dehyd},nC_7}$; eq 10) and Measured First-Order Rate Constants for 24DMP Consumption[a] ($\psi_{\mathrm{total},24}$; eq 26) on MFI Zeotypes (X-MFI, where X = Al, Ga, Fe, B)

acid	$k_{\mathrm{isom},nC_7}K_{\mathrm{prot},nC_7}K_{\mathrm{dehyd},nC_7}$/(H+ ks)$^{-1}$	$\psi_{\mathrm{total},24}$/(H+ ks)$^{-1}$ [a]
Al-MFI-1	1850 (±40)	2190 (±65)
Al-MFI-2	2320 (±170)	484 (±70)
Ga-MFI	206 (±7.5)	127 (±3.5)
Fe-MFI	78.5 (±5.0)	74.0 (±7.9)
B-MFI	0.20 (±0.008)	6.8 (±0.05)

[a]Measured 24DMP consumption rate constants ($\psi_{\mathrm{total},24}$ values) reflect kinetically relevant concentration gradients of reactant alkenes (Section 3.3).

entropies; transition state enthalpies, and thus transition state electronic energies, compensate for any differences in entropic effects at the moderate temperatures of isomerization reactions ($\langle\Delta H^‡_{\mathrm{app},nC_7}\rangle \gg T\langle\Delta S^‡_{\mathrm{app},nC_7}\rangle$, where $\langle\Delta H^‡_{\mathrm{app},nC_7}\rangle$, and $\langle\Delta S^‡_{\mathrm{app},nC_7}\rangle$ are transition state activation enthalpies and entropies, respectively).[8] The dashed line in Figure 3 thus represents the extent to which activation barriers "sense" the acid strength of these MFI zeotypes:

$$\frac{\partial(\ln(k_{\mathrm{isom},nC_7}K_{\mathrm{prot},nC_7}K_{\mathrm{dehyd},nC_7}))}{\partial(\mathrm{DPE})} = -\frac{1}{k_BT}\frac{\partial(\langle E_{\mathrm{app},nC7}\rangle)}{\partial(\mathrm{DPE})} \tag{15}$$

The constant and subunity slope of this regressed line ($\partial(\langle E_{\mathrm{app},nC_7}\rangle)/\partial(\mathrm{DPE}) = 0.69$) indicates that activation barriers reflect transition states that recover a similar fraction of the energy required to separate charge in the deprotonation of the solid acid on MFI zeotypes with different heteroatoms.

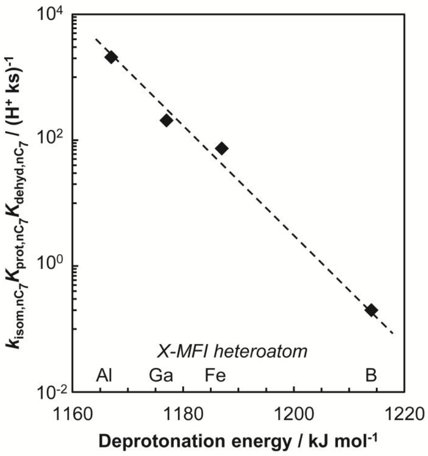

Figure 3. Measured first-order rate constants for *n*-heptane isomerization (per H^+; $k_{\mathrm{isom},nC_7}K_{\mathrm{prot},nC_7}K_{\mathrm{dehyd},nC_7}$; eq 10) as a function of X-MFI deprotonation energy (where X = Al, Ga, Fe, B) (548 K). The dashed line represents the regressed exponential fit of the nC_7 rate constants (eq 15).

The effects of DPE on first-order rate constants (Figure 3) are interpreted here using thermochemical cycles[46] that seek to dissect activation energies into a sequence of hypothetical steps (Scheme 4); these steps are chosen for convenience and exploit the state function character of thermodynamic properties. The ion-pair transition state (with its formation free energy taken with respect to gaseous precursors, $\langle E_{\mathrm{app},nC_7}\rangle$) forms by (i) deprotonating the acid (DPE); (ii) forming the gaseous analogue of the transition state carbocation (proton affinity, $\langle E_{\mathrm{prot},nC_7}\rangle$); and (iii) bringing the carbocation and the conjugate anion at their respective interacting positions in the transition state structure ($\langle E_{\mathrm{int},nC_7}\rangle$). The cation–anion interaction energies at the transition state ($\langle E_{\mathrm{int},nC_7}\rangle$) can be further dissected into components that account for (i) dispersive host–guest interactions (van der Waals interactions, $\langle E_{\mathrm{vdw},nC_7}\rangle$);

Scheme 4. Thermochemical Cycle for the Formation of the *n*-Heptane Isomerization Transition State (to 2-Methylhexane; with Apparent Activation Energy $E_{\mathrm{app},nC7}$) on MFI Zeotypes

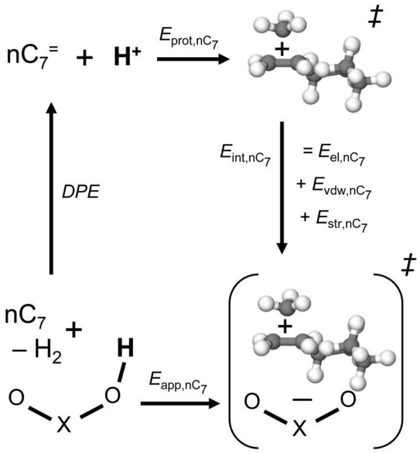

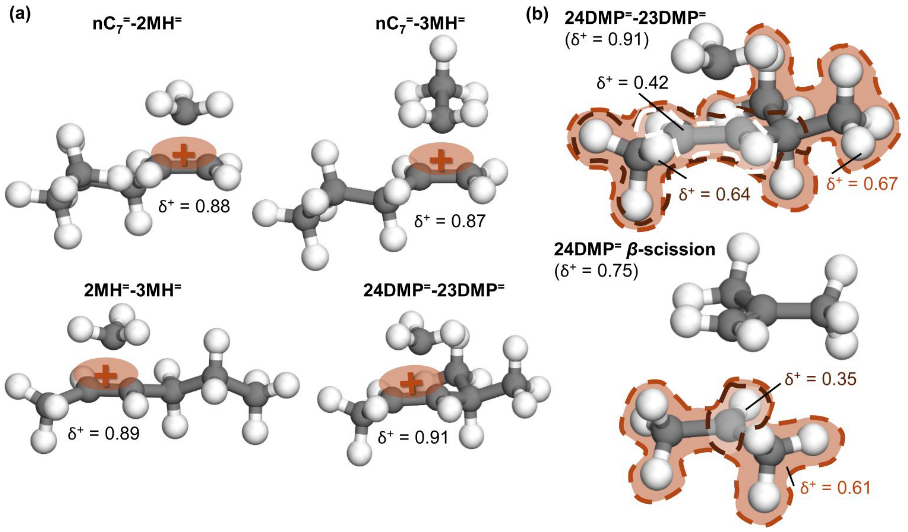

Figure 4. (a) Alkyl-substituted cyclopropyl carbenium ions at the transition states that mediate the isomerization of various alkenes. Partial charges (Section 2.3) represent the total positive charge on each carbocation; the conjugate anion has the corresponding amount of negative charge. (b) Charge distributions at 2,4-dimethylpentene transition states for isomerization (top) and β-scission steps (bottom). Charges indicate the sum for all atoms contained within the colored dashed lines. Structures were converged at the T12-O20(H) location in MFI (VASP RPBE + D3(BJ)) then excised from the framework for visual clarity.

(ii) structural deformations of the framework and the organic carbocation ($\langle E_{\mathrm{str},n\mathrm{C}_7}\rangle$); and (iii) electronic interactions ($\langle E_{\mathrm{el},n\mathrm{C}_7}\rangle$) to give $\langle E_{\mathrm{app},n\mathrm{C}_7}\rangle$ as the sum of these contributions:

$$\langle E_{\mathrm{app},n\mathrm{C}_7}\rangle = \mathrm{DPE} + \langle E_{\mathrm{prot},n\mathrm{C}_7}\rangle + \langle E_{\mathrm{el},n\mathrm{C}_7}\rangle + \langle E_{\mathrm{vdw},n\mathrm{C}_7}\rangle + \langle E_{\mathrm{str},n\mathrm{C}_7}\rangle \qquad (16)$$

The effects of acid strength on activation energies are then given by the derivative of this equation with respect to DPE

$$\frac{\partial\langle E_{\mathrm{app},n\mathrm{C}_7}\rangle}{\partial\mathrm{DPE}} = \frac{\partial\mathrm{DPE}}{\partial\mathrm{DPE}} + \frac{\partial\langle E_{\mathrm{prot},n\mathrm{C}_7}\rangle}{\partial\mathrm{DPE}} + \frac{\partial\langle E_{\mathrm{el},n\mathrm{C}_7}\rangle}{\partial\mathrm{DPE}} + \frac{\partial\langle E_{\mathrm{vdw},n\mathrm{C}_7}\rangle}{\partial\mathrm{DPE}} + \frac{\partial\langle E_{\mathrm{str},n\mathrm{C}_7}\rangle}{\partial\mathrm{DPE}} = 1 + \frac{\partial\langle E_{\mathrm{el},n\mathrm{C}_7}\rangle}{\partial\mathrm{DPE}} \qquad (17)$$

$\langle E_{\mathrm{prot},n\mathrm{C}_7}\rangle$ is a property of the gaseous species and thus independent of DPE ($\frac{\partial(\langle E_{\mathrm{prot},n\mathrm{C}_7}\rangle)}{\partial(\mathrm{DPE})} = 0$). The $\langle E_{\mathrm{str},n\mathrm{C}_7}\rangle$ and $\langle E_{\mathrm{vdw},n\mathrm{C}_7}\rangle$ terms are unaffected by DPE because cation−anion distances at the transition states vary negligibly with changes in the stability of the conjugate anion (distances for nC$_7^=$-2MH$^=$ and nC$_7^=$-3MH$^=$ transition states given in section S4, SI), and the confining environment is the same for MFI structures with different framework heteroatoms.

Measured first-order rate constants (Figure 3) are accurately described by a $\frac{\partial(\langle E_{\mathrm{app},n\mathrm{C}_7}\rangle)}{\partial(\mathrm{DPE})}$ value that is constant and smaller than unity (0.69; Figure 3). This slope corresponds to a $\frac{\partial\langle E_{\mathrm{el},n\mathrm{C}_7}\rangle}{\partial\mathrm{DPE}}$ value of −0.31, with the sign indicative of ion-pair interactions that *recover* a fraction of the energy required to separate the proton from the conjugate anion. The latter process cleaves O−H bonds that are largely covalent, with only minor contributions by Coulombic interactions mediated by classical electrostatic forces.[47,48] Transition states, in contrast, are essentially ion pairs (0.87−0.91 charges at each ion; QUAMBO, Section 2.3, Figure 4a) that interact via electrostatic forces. The minimal covalent contribution for transition states preclude the more complete recovery of the DPE upon forming ion pairs at the isomerization transition states.

The recovery of the ionic part of DPE by isomerization transition states is attenuated by the charge reorganization that delocalizes the positive charge upon proton transfer.[49] The carbocations at nC$_7^=$ isomerization transition states are alkyl-substituted cyclopropyl carbenium ions that differ from each other only in the location of their alkyl substituents as they lead to the formation of the different product isomers (2MH$^=$ and 3MH$^=$; DFT-derived structures in Figure 4a); all transition states delocalize charge almost uniformly among the three C atoms that compose the cyclopropyl ring. In contrast, the conjugate anion formed upon framework deprotonation remains very localized at the trivalent heteroatom for heterosilicate frameworks.[7] As a result, such a localized charge interacts much less effectively with the dispersed positive charge at the carbocations. The small fraction of the DPE (0.31) recovered by the ensemble of nC$_7^=$ isomerization transition states thus reflects both minimal covalency at transition states and the ineffective Coulombic interactions between carbocations and conjugate anions.

The mechanistic assessment of the effects of acid strength on nC$_7$ isomerization rate constants is extended in what follows to a description of isomerization selectivities. The formation energy for the ensemble of nC$_7^=$ isomerization transition states ($\langle E_{\mathrm{app},n\mathrm{C}_7}\rangle$) includes the energies of formation of all transition states that can form all distinct primary 2MH* and 3MH* products from each respective heptoxide precursor. These values determine nC$_7$ isomerization rate constants ($k_{\mathrm{isom},n\mathrm{C}_7}K_{\mathrm{prot},n\mathrm{C}_7}K_{\mathrm{dehyd},n\mathrm{C}_7}$, eq 10). A mechanistic interpretation of the effects of acid strength on isomerization selectivity would require independent measurements of the rate constants for the formation of the 2MH and 3MH primary products; these data are experimentally inaccessible because of the rapid interconversion of these two skeletal isomers. The lumped $k_{\mathrm{isom},n\mathrm{C}_7}K_{\mathrm{prot},n\mathrm{C}_7}K_{\mathrm{dehyd},n\mathrm{C}_7}$ parameter reflects the combined rate constants for the formation of each skeletal isomer product (where *j* indicates 2MH and 3MH here):

$$k_{\mathrm{isom},nC_7}K_{\mathrm{prot},nC_7}K_{\mathrm{dehyd},nC_7} = \sum_j k_{\mathrm{isom},nC_7,j}K_{\mathrm{prot},nC_7}K_{\mathrm{dehyd},nC_7} \tag{18}$$

The effect of DPE on these rate constants is then given by

$$\frac{\partial(k_{\mathrm{isom},nC_7}K_{\mathrm{prot},nC_7}K_{\mathrm{dehyd},nC_7})}{\partial(\mathrm{DPE})} = \sum_j \frac{\partial(k_{\mathrm{isom},nC_7,j}K_{\mathrm{prot},nC_7}K_{\mathrm{dehyd},nC_7})}{\partial(\mathrm{DPE})} \tag{19}$$

eqs 15 and 19, taken together, lead to a relation between the rate constants and activation energies:

$$-k_BT\frac{\partial(\ln(k_{\mathrm{isom},nC_7}K_{\mathrm{prot},nC_7}K_{\mathrm{dehyd},nC_7}))}{\partial(\mathrm{DPE})} = \sum_j S_{nC_7,j,0}\frac{\partial(\langle E_{\mathrm{app},nC_7,j}\rangle)}{\partial(\mathrm{DPE})} \tag{20}$$

Thus, selectivities become independent of acid strength when the barriers for the formation of all primary products depend similarly on DPE. The constant nature of the $-k_BT\frac{\partial(\ln(k_{\mathrm{isom},nC_7}K_{\mathrm{prot},nC_7}K_{\mathrm{dehyd},nC_7}))}{\partial(\mathrm{DPE})}$ term (Figure 3) indicates that $\frac{\partial(\langle E_{\mathrm{app},nC_7,j}\rangle)}{\partial(\mathrm{DPE})}$ values for $2MH^=$ and $3MH^=$ are similar and that intrinsic selectivities ($S_{nC_7,j,0}$, eq 5) are therefore independent of acid strength. The intrinsic rates for 2MH and 3MH formation cannot be measured individually because of their fast equilibration;[8] consequently, DFT-derived differences in energy between the transition states that mediate $nC_7^=$ conversion to $2MH^=$ and $3MH^=$ are used next to probe the effects of acid strength on the intrinsic formation rates of these two primary methyl-branched isomer products.

$nC_7^=$ forms $2MH^=$ and $3MH^=$ via steps mediated by several distinct transition states, which convert each different nC_7* attachment isomer to all possible 2MH* and 3MH* attachment isomers. DFT methods were used to isolate the lowest energy transition state for the formation of each skeletal isomer product because such a structure will contribute most significantly to the energy of the ensemble of transition states (eq 11). These structures were converged at the T20-O(12)H location in MFI voids with Al, Ga, Fe, or B heteroatoms using functionals that account for dispersive forces (Section 2.3). Figure 4 shows the carbocation structures at these transition states and the charges at the cation and the conjugate anion. Transition states consist of alkyl-substituted cyclopropyl carbenium ions ($\delta^+ = 0.87-0.88$; QUAMBO, Section 2.3) formed by nearly complete transfer of protons from the frameworks.

Figure 5 shows the DFT-derived energies for the formation of $2MH^=$ and $3MH^=$ transition states (from bare protons, nC_7, and H_2) as a function of DPE in X-MFI samples; these represent the activation barriers that determine the respective first-order rate constants for $2MH^=$ and $3MH^=$ formation. $2MH^=$ formation activation barriers are smaller than those for $3MH^=$ formation on each acid, consistent with the preferential formation of $2MH^=$ over $3MH^=$ and with their subsequent equilibration in secondary reactions during nC_7 isomerization reactions on Al-MCM-41 mesoporous acids.[8] Both activation barriers depend similarly on DPE, with their slopes having values of 0.84 and 0.85 for $2MH^=$ formation and $3MH^=$ formation, respectively; such similar slopes indicate that the ratios of the respective rate constants for the formation of $2MH^=$ and $3MH^=$ are independent of DPE, as concluded indirectly from the linear nature of the data in Figure 3. The activation barriers are lower for $nC_7^=$-$2MH^=$ than for $nC_7^=$-$3MH^=$, with their constant difference for all acids indicative of the different stability of their respective carbocations (E_{prot}), which influence intrinsic selectivities (eq 16) but do not sense acid strength.

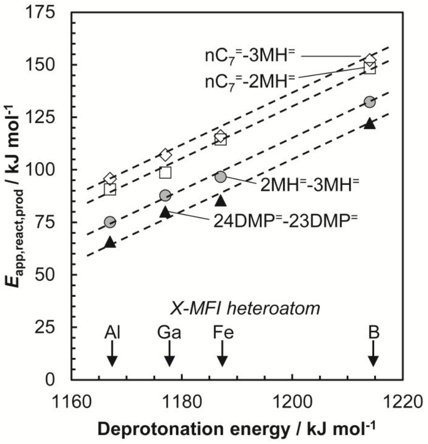

Figure 5. DFT-derived activation barriers for $nC_7^=$-$3MH^=$ (diamonds), $nC_7^=$-$2MH^=$ (squares), $2MH^=$-$3MH^=$ (circles), and $24DMP^=$-$23DMP^=$ (triangles), taken with respect to bare protons and gas-phase reactant alkanes and H_2, as a function of deprotonation energy of MFI zeotypes of different strength (RPBE PAW D3(BJ); MFI-T12-O(20)H). Dashed lines represent linear trends.

The similar effects of DPE on the activation barriers for the formation of $2MH^=$ and $3MH^=$ (from $nC_7^=$) indicate that their respective transition states recover a similar fraction of the electrostatic energy required to deprotonate the solid acid. The thermochemical cycle in Scheme 4, together with eq 17, indicates that such interaction energies reflect transition state stabilization via electronic interactions that are predominantly Coulombic in nature for these ion-pair transition states. DFT-derived charges for these carbocations (Figure 4b; QUAMBO, Section 2.3) show that charges are distributed similarly throughout each of these two transition state carbocations: the positive charge ($\delta^+ = 0.87-0.88$) is dispersed uniformly across the three C atoms of the cyclopropyl ring ($\delta^+ = 0.20-0.25$ at each carbon), while alkyl substituents remain nearly uncharged ($\delta^+ = 0.00-0.12$), irrespective of their attachment point at the C atoms in the cyclopropyl ring (as discussed later in this section). Such similar charge distributions lead to transition state carbocations for $nC_7^=$ isomerization to $2MH^=$ and $3MH^=$ that interact with the localized negative charges at conjugate anions via similar Coulombic interactions. Consequently, these ion-pair transition states recover to the same extent the electrostatic energy required to deprotonate the acid.

DFT treatments also allow fundamental inquiries into the effects of acid strength on secondary reactions during $nC_7^=$ isomerization, such as $2MH^=$ conversion to $3MH^=$ and $24DMP^=$ isomerization to $23DMP^=$, in which a methyl group shifts along the backbone. These reactions are mediated by ion-pair transition states similar to those that mediate $nC_7^=$-$2MH^=$ and $nC_7^=$-$3MH^=$ isomerization and that also consist of alkyl-substituted cyclopropyl carbenium ions (structures shown in Figure 4a) interacting with the conjugate anion of the solid acid. The charge distributions at these transition state carbocations are nearly identical to those for the primary isomerization transition state carbocations (SI, section S4; QUAMBO, Section 2.3), as expected from their analogous cyclopropyl carbenium ion backbones. Such similar charge distributions at these carbocations suggest that the Coulombic interactions at the ion-pair transition states will be similar to each other and to the transition states forming 2MH$^{=}$ and 3MH$^{=}$ from *n*C$_7^{=}$. These transition states are therefore expected to recover a similar fraction of deprotonation energy to each other and to *n*C$_7^{=}$-2MH$^{=}$ and *n*C$_7^{=}$-3MH$^{=}$ transition states, and the energies of all of these transition states should change with the same sensitivity to deprotonation energy.

DFT-derived energies for the formation of 2MH$^{=}$-3MH$^{=}$ and 24DMP$^{=}$-23DMP$^{=}$ isomerization transition states (carbocation structures in Figure 4a) from bare protons, H$_2$, and the respective gaseous alkanes (2MH for 2MH$^{=}$-3MH$^{=}$ and 24DMP for 24DMP$^{=}$-23DMP$^{=}$) are shown in Figure 5 as a function of the DPE of each zeotype. These transition state energies increase as acid sites weaken with the same sensitivity to DPE for 2MH$^{=}$-3MH$^{=}$ and 24DMP$^{=}$-23DMP$^{=}$ reactions (Figure 5; 0.84 and 0.85, respectively); these slopes are also similar to those for *n*C$_7^{=}$-2MH$^{=}$ and *n*C$_7^{=}$-3MH$^{=}$ reactions (Figure 5; 0.84 and 0.85, respectively). These similar slopes, which reflect the effectiveness of Coulombic interactions at ion-pair transition states (eq 17), are consistent with expectations based on the nearly identical charge distributions at all alkyl-substituted cyclopropyl carbenium ions (Figure 4b for 24DMP$^{=}$-23DMP$^{=}$; SI, section S4 for others).

Transition state energies for *n*C$_7^{=}$ isomerization (to 2MH$^{=}$ or 3MH$^{=}$), 2MH$^{=}$ isomerization to 3MH$^{=}$, and 24DMP$^{=}$ isomerization to 23DMP$^{=}$ as a function of DPE have the same slopes and are parallel lines at every DPE (Figure 5), with different *y*-intercept values; transition state energies for the conversion of 2MH$^{=}$ to 3MH$^{=}$ are smaller than those for *n*C$_7^{=}$ isomerization to either primary product; activation barriers for 24DMP$^{=}$-23DMP$^{=}$ conversion are smaller than those for 2MH$^{=}$-3MH$^{=}$ conversion (by ∼10 kJ/mol) for each zeotype. These constant differences in transition state energies at all DPE values reflect the greater stability of 24DMP$^{=}$-derived methyl shift transition states compared to those derived from 2MH$^{=}$, as a result of the higher proton affinity of 24DMP$^{=}$-23DMP$^{=}$ transition state carbocations compared to 2MH$^{=}$-3MH$^{=}$ transition state carbocations (E_{prot}, eq 16).[50] These transition state carbocations vary in their location and branching of alkyl substituents on the cyclopropyl carbenium ion backbone. The 24DMP$^{=}$-23DMP$^{=}$ and 2MH$^{=}$-3MH$^{=}$ transition state carbocations both have one methyl substituent and one propyl substituent on the two-C backbone of the cyclopropyl carbenium ion (the two C closest to the conjugate anion). The isopropyl group of the 24DMP$^{=}$-23DMP$^{=}$ transition state carbocation is more electron-donating than the *n*-propyl group of the 2MH$^{=}$-3MH$^{=}$ transition state carbocation; as a result, the former transition state carbocation is more stable and has a higher E_{prot} than the latter.

*n*C$_7^{=}$-2MH$^{=}$ and *n*C$_7^{=}$-3MH$^{=}$ transition state carbocations each only have one *n*-alkyl substituent on the two-C backbone of the cyclopropyl carbenium ions; the former has an *n*-butyl group, while the latter has an *n*-propyl group and an additional methyl substituent at the passing C of the cyclopropyl ring. The *n*-butyl group of the *n*C$_7^{=}$-2MH$^{=}$ transition state carbocation is more electron-donating than the *n*-propyl group of the *n*C$_7^{=}$-3MH$^{=}$ transition state carbocation, resulting in the observed differences in E_{prot}. Surprisingly, the methyl group at the passing C of the latter carbocation does not increase proton affinity.

Alkene isomerization selectivities that are independent of acid strength and that solely reflect carbocation proton affinities have been reported for C$_6$ alkene isomerization[51] and methylcyclohexene ring contraction[11] on stronger mesoporous solid acids (Keggin-type polyoxometalate clusters of varying central atom, DPE = 1087−1143 kJ mol^{-1}, supported on SiO$_2$). The amount and location of positive charge were similar among all of the alkyl-substituted cyclopropyl carbenium ions that mediate the different C$_6$ alkene isomerization routes, irrespective of the position of alkyl substituents. As a result, these ion-pair transition states recover similar fractions of the deprotonation energy through Coulombic interactions. Similar conclusions were reached for the series of alkyl-substituted bicyclo[3.1.0]-hexyl carbenium ions mediating methylcyclohexene ring contraction reactions. Again, these ion-pair transition states recover similar fractions of deprotonation energy because the alkyl-substituted bicyclo[3.1.0]hexyl carbenium ions dispersed positive charge to a similar extent.

The similar amount and distribution of charge in the cationic moieties at the transition states that mediate all primary and secondary skeletal isomerization events in reactions of *n*C$_7$ lead to selectivities (ratios of rate constants) that are independent of acid strength. The primary and secondary events involved in reactions of 24DMP involve skeletal rearrangements that are mediated by the same transition states involved in primary and secondary reactions with *n*C$_7$ reactants, and their relative rates are also insensitive to DPE. In practice, the measurement of rates of single-site primary isomerization and *β*-scission events requires the suppression of diffusion-enhanced secondary reactions that also influence the relative concentrations of primary and secondary products; these diffusional effects depend on the Thiele moduli (eq 13) associated with the secondary rearrangements of the product alkenes[8,11] and become most severe for the most active sites, whether rendered so by their acid strength or by van der Waals contacts between transition states and the void walls. In what follows, we probe intrinsic selectivities for *β*-scission and isomerization for 24DMP reactants on aluminosilicates of similar acid strength but different frameworks by introducing temporal variations in their Thiele moduli as the number of acid sites increases during the desorption of preadsorbed NH$_3$ titrants (Section 2.2), a method that allows accurate extrapolations to the initial stages of titrant desorption, during which intracrystalline gradients are least severe and selectivities reflect the products formed in a single sojourn at an active site.

3.2. 2,4-Dimethylpentane Isomerization and *β*-Scission and the Effects of Aluminosilicate Framework Structure on Selectivity.

Both isomerization and *β*-scission products can form directly from 24DMP$^{=}$, but the primary isomers formed can also undergo secondary reactions before egressing from porous aggregates or crystallites. Scheme 1b shows the 2,4-dimethylpentane reaction network. 2,3-Dimethylpentane (23DMP; methyl shift), equimolar amounts of propane and isobutane (*β*-scission), and 2MH, 3MH, *n*C$_7$, 2,2-dimethylpentane (22DMP), and 3,3-dimethylpentane (33DMP) isomers were detected as reaction products. 22DMP and 33DMP are combined here and treated as 23DMP formation events because such quaternary hydrocarbons form via secondary isomerization of 23DMP alkenes but not directly from 24DMP alkenes or other primary isomer

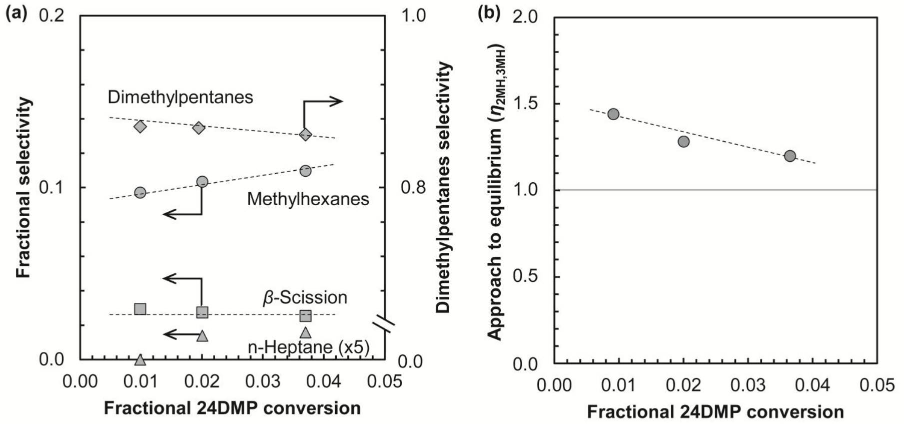

Figure 6. (a) Fractional product selectivities to dimethylpentanes (diamonds, right axis), methylhexanes (circles, left axis), *n*-heptane (triangles, left axis; multiplied by 5), and *β*-scission (squares, left axis) and (b) approach to equilibrium for 2-methylhexane with respect to 3-methylhexane ($\eta_{2MH,3MH}$, eq 2) during 2,4-dimethylpentane reactions on physical mixtures of Pt/SiO_2 and MCM-41 as a function of reactant conversion ((24DMP)/(H_2) = 0.005, 100 kPa H_2, 548 K; reactant conversion varied through changes in space velocity). Dashed lines in (a) and (b) represent trends; the horizontal line in (b) indicates unity, the definition of full equilibration.

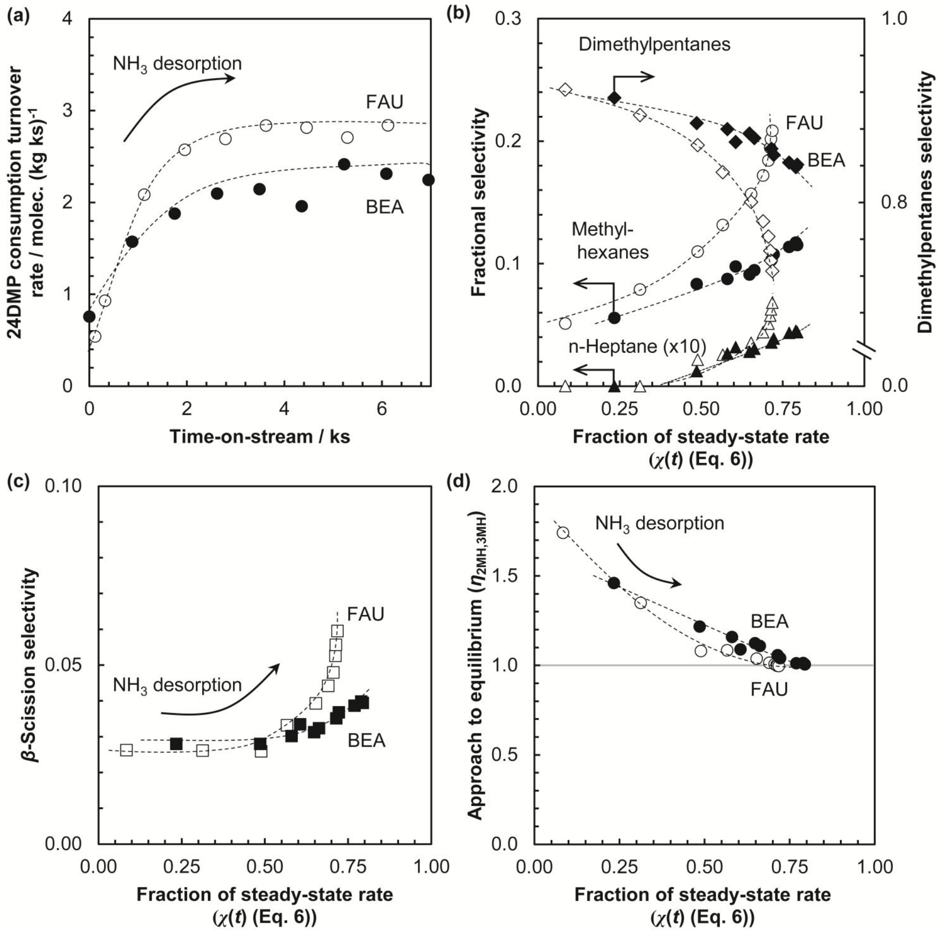

Figure 7. (a) 2,4-Dimethylpentane consumption turnover rates as a function of time-on-stream during NH_3 desorption on physical mixtures of Pt/SiO_2 and FAU (open) and BEA (filled). (b) Selectivities to dimethylpentanes (diamonds, right axis), methylhexanes (circles, left axis), *n*-heptane (circles, left axis; × 10), and (c) *β*-scission products, and (d) approach to equilibrium for 2-methylhexane with respect to 3-methylhexane ($\eta_{2MH,3MH}$, eq 2) as a function of fractional steady-state rate ($\chi(t)$, eq 6) varied by NH_3 desorption during 2,4-dimethylpentane reactions on physical mixtures of Pt/SiO_2 and FAU (white) and BEA (black) (0.005 (24DMP)/(H_2) molar ratio, 100 kPa H_2, 548 K). The horizontal line in (d) represents unity. Dashed curves represent trends.

DOI: 10.1021/acs.jpcc.8b08460
J. Phys. Chem. C 2018, 122, 25475−25497

products (2MH and 3MH alkenes);[51] the alkyl-substituted cyclopropyl carbenium ions that mediate methyl shifts can only move one methyl group during each reactive surface sojourn. 2MH and 3MH can form as primary products via a single chain-lengthening event from 24DMP, but their rapid interconversion leads to equilibrated 2MH−3MH mixtures at all conditions; they are therefore considered as lumped methylhexanes (MH) that can form nC_7 and 23DMP in subsequent surface sojourns.

Figure 6a shows the product selectivities from 24DMP reactions on mesoporous Al-MCM-41 as a function of the fractional 24DMP conversion, varied through changes in bed residence time. 23DMP, MH, and β-scission products form with nonzero selectivities at short bed residence times, consistent with their direct formation from alkenes derived from 24DMP reactants. The asymptotic nC_7 selectivity (as conversion approaches zero) is near zero and increases with increasing bed residence time, as expected from the secondary nature of nC_7 products. Secondary conversion of 23DMP to MH leads to 23DMP selectivities that decrease and MH selectivities that increase with increasing residence time. β-Scission selectivities were not affected by residence time, consistent with β-scission events that predominantly involve 24DMP-derived alkenes and that occur in parallel with the isomerization of such alkenes in primary reactions. Figure 6b shows the approach to equilibrium parameters for 2MH conversion to 3MH ($\eta_{2MH,3MH}$, eq 2; $K_{2MH,3MH}$ = 0.87 at 548 K[22]). These $\eta_{2MH,3MH}$ parameters are initially larger than unity but decrease as bed residence time increases, indicating that 2MH is the predominant initial isomer formed from 24DMP-derived alkenes but then converts via methyl shifts to 3MH along the Al-MCM-41 catalyst bed even at very low conversions and short residence times.

Methylhexane products form on Al-MCM-41 acids via a single reactive sojourn or through subsequent reactions of primary products that desorb but then react further along the catalyst bed; the Al-MCM-41 mesopores (2.5 nm diameter) allow facile molecular diffusion and impose only weak confinement effects on reactivity.[8] As a result, the primary alkene isomers can hydrogenate at the metal function present outside the porous acid domains before secondary rearrangements can occur within the given acid domain in which they first formed.

In contrast, 24DMP product selectivities on microporous acids were essentially unaffected by bed residence time (section S5, SI; SFH as an illustrative example; selectivities to MH varied from 0.20 to 0.22, to 23DMP from 0.63 to 0.65, to β-scission products from 0.08 to 0.09, and to nC_7 from 0.01 to 0.02). The nC_7 selectivities were nonzero (∼0.01−0.02) at all reactant conversions on SFH, even though nC_7 could only have formed via subsequent reactions of the isoalkenes formed as primary products from 24DMP-derived alkenes (2MH and 3MH). Nonzero selectivities to secondary products and the insensitivity of all selectivities to bed residence times reflect diffusion-enhanced secondary reactions that occur within the acid domain in which the primary isoalkenes first formed. Such effects reflect, in turn, strong diffusional hurdles combined with higher turnover rates, both conferred by voids of molecular size in these microporous frameworks.

The contributions from diffusion-enhanced secondary reactions within a given zeolite crystal to measured selectivities depend on the intracrystalline residence times ($\tau_{cryst,j}$) of each product alkene j within a given zeolite framework:[8]

$$\tau_{cryst,j} = \frac{\rho_{H^+} R^2}{D_j} = \phi_j^2/\alpha_j \tag{21}$$

where the nomenclature is the same as in eq 13 but now reflects reactive and diffusional properties of the product (rather than of the reactant) alkenes. Small $\tau_{cryst,j}$ values minimize the extent to which secondary interconversions occur and favor the detection of primary products. The desorption of NH_3 titrants preadsorbed on acid sites causes a temporal increase in ρ_{H^+} and thus in $\tau_{cryst,j}$ (Section 2.2). This method was previously developed and reported for reactions of nC_7 on aluminosilicates, for which it was used to assess the rates of formation of products in single-sojourn events.[8]

Figure 7a shows that 24DMP consumption rates on FAU and BEA increase as the number of accessible protons increases during NH_3 desorption at 548 K and ultimately approach those on the fresh untitrated samples (after ∼10 ks). 24DMP conversion rates reflect the intrinsic reactivity and the number of acid sites combined with any diffusional effects that impose intracrystalline gradients of 24DMP-derived alkenes (Section 3.3). These concentration gradients become systematically more severe as NH_3 desorbs because of the higher volumetric depletion rates of alkene reactants with increasing density of intracrystalline protons. Consequently, the ratio of measured rates to steady-state rates ($\chi(t)$; eq 6) depends linearly on the number of protons that become accessible during the initial stages of NH_3 desorption because during such initial stages, ρ_{H^+} values are smallest and 24DMP alkene concentration gradients least severe. The dependence of $\chi(t)$ values on ρ_{H^+} becomes sublinear (and ultimately approaches a $\rho_{H^+}{}^{0.5}$ dependence, as demonstrated by the asymptotic behavior of eq 14 at large values of ϕ_i) as concentration gradients become increasingly severe as the titrant desorbs, but even then, $\chi(t)$ remains a directional indicator of monotonic changes in ρ_{H^+} and of the effects of ρ_{H^+} on the extent to which diffusion-enhanced secondary reactions influence isomerization and β-scission selectivity.

Figure 7b shows isomer selectivities as a function of $\chi(t)$ as the NH_3 titrants desorb from the acid sites in FAU and BEA aluminosilicates. nC_7 products are initially undetectable, but their selectivity increases with increasing ρ_{H^+} and $\chi(t)$ increase. Initial MH selectivities are nonzero (∼0.05) and increase (to 0.12−0.20) as NH_3 desorbs, while the selectivity to 23DMP is also initially nonzero (∼0.92) but decreases with time as NH_3 desorbs (to 0.73−0.84). These trends show that (i) nC_7 forms only through secondary reactions of primary MH isomers within zeolite crystallites; (ii) 23DMP and MH can form directly from 24DMP; and (iii) 23DMP forms MH (and MH forms nC_7) in secondary reactions.

These conclusions, based on intracrystalline residence times that increase monotonically as NH_3 desorbs, are identical to those derived from the observed effects of bed residence time on mesoporous Al-MCM-41 aluminosilicates, for which large mesopores minimize confinement effects on reactivity and allow rapid molecular diffusion, thus avoiding intraparticle secondary reactions and allowing their detection instead along the catalyst bed (Figure 6a). The $\eta_{2MH,3MH}$ values on FAU and BEA (Figure 7c) were above unity at small ρ_{H^+} and $\chi(t)$ values and then approached unity, as also observed with changes in bed residence time on the mesoporous Al-MCM-41 acids, because of the preferential formation of 2MH (over 3MH) from 24DMP and its conversion to 3MH in fast secondary isomerization events.

DOI: 10.1021/acs.jpcc.8b08460
J. Phys. Chem. C 2018, 122, 25475−25497

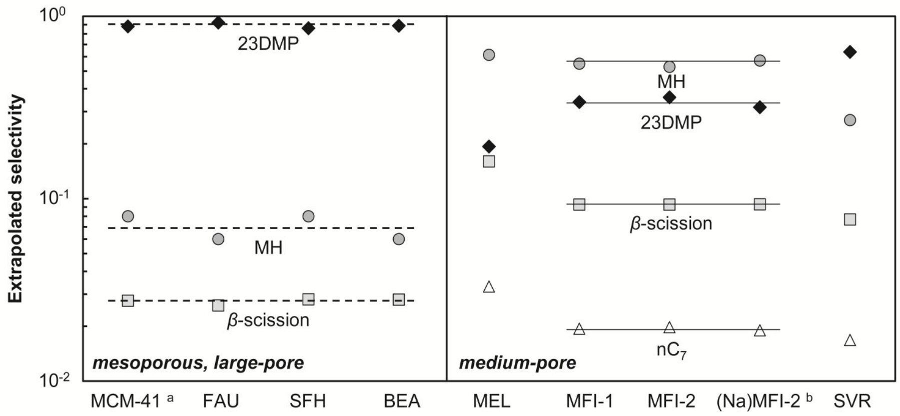

Figure 8. 2,3-Dimethylpentane (diamonds), methylhexanes (circles), *n*-heptane (triangles), and β-scission (squares) selectivities extrapolated to initial $\chi(t)$ values during NH_3 desorption ($S_{24,\mathrm{prod},0}$, eq 5) on aluminosilicates (0.005 (24DMP/H_2) molar ratio, 100 kPa H_2, 548 K). Dashed lines represent average values for mesoporous and large-pore aluminosilicates, and solid lines represent average values for MFI materials. [a]Values for MCM-41 extrapolated to zero bed residence time. [b]Values for (Na)MFI-2 during steady-state reaction.

β-Scission selectivities (Figure 7d) extrapolated to low ρ_{H^+} ($\chi(t) \rightarrow 0$) are nearly identical on FAU and BEA (0.026 and 0.028, respectively) and increase with increasing ρ_{H^+} as NH_3 desorbs. These data indicate that the isomers formed from 24DMP-derived alkene reactants can undergo β-scission at rates that are comparable to the primary β-scission of 24DMP-derived alkenes, in apparent contradiction to β-scission selectivities that were unaffected by bed residence time on Al-MCM-41 (Figure 6a); these latter data indicate that β-scission occurs predominantly for 24DMP-derived alkenes instead of their isomerization products. The higher β-scission selectivities detected on microporous acids as NH_3 desorbs do not reflect significant secondary β-scission of isomerization product but arise instead from strong intracrystalline gradients of 24DMP-derived alkene regioisomers (as discussed in SI, section S6), which lead to re-formation of 24DMP alkenes from other products within inner regions of acid domains where 24DMP concentrations become lower than those in equilibrium with its isomer products. $24DMP^=$ diffuses more slowly and is more reactive than the isomers it forms, leading to very low $24DMP^=$ concentrations throughout the inner regions in zeolite crystallites. The methylhexene isomers that form from $24DMP^=$, for example, diffuse faster and react more slowly than $24DMP^=$,[8] thus allowing their local intracrystalline concentrations to exceed those that would be present in equilibrium with $24DMP^=$ within the inner regions of zeolite crystallites. As a result, $24DMP^=$ molecules re-form and can undergo β-scission via processes that become more consequential for the stronger $24DMP^=$ concentration gradients that prevail as NH_3 desorbs and $\chi(t)$ increases. These diffusional enhancements of β-scission reactions only occur within a single acid domain and not in reactions further down the catalyst bed because the residence times of product alkenes vary within zeolite crystallites ($\tau_{\mathrm{cryst},j}$) but their residence times within the bed are similar. Extrapolation of selectivities to zero ρ_{H^+} and $\chi(t)$ values thus suppresses the contributions from diffusion-enhanced secondary reactions occurring on the length scale of single crystallites.

Figure 8 shows 23DMP, nC_7, and β-scission selectivities extrapolated to the initial stages of NH_3 desorption ($\rho_{H^+}, \chi(t) \rightarrow 0$) on zeolites (FAU, SFH, BEA, MEL, MFI, SVR) and to zero bed residence times on Al-MCM-41. Secondary nC_7 isomers were not detected on Al-MCM-41, FAU, SFH, or BEA, indicative of intracrystalline residence times that are sufficiently short to preclude its formation via secondary reactions within a single acid domain. These mesoporous and large-pore solid acids gave similar initial 23DMP, MH, and β-scission selectivities, in contradiction with proposals that zeolites are stronger acids than mesoporous aluminosilicates and that stronger acids favor β-scission over isomerization events.[12−15] These aluminosilicates contain acid sites of similar strength[16,17] but which reside within different void structures that stabilize transition state carbocations by van der Waals contacts; such stabilization by confinement leads to very large effects of the void structure on turnover rates (e.g., 1000-fold for nC_7 isomerization at 548 K among these aluminosilicates[8]). The same voids and channels that confer such confinement effects on reactivity impose the diffusional hurdles that give selectivities that arise not only from single sojourns but also from large contributions from subsequent reactive events of primary products.

The stabilization of transition states by van der Waals contacts depends sensitively on the fit (in size and shape) between the void and the carbocationic guest; the effectiveness of such contacts is given by an interaction energy (E_{vdw}) that was previously calculated for the carbocations involved in $nC_7^=$ isomerization (to $2MH^=$ and $3MH^=$), in $24DMP^=$ isomerization (to $23DMP^=$), and in $24DMP^=$ β-scission in FAU, SFH, BEA, and MFI; these interaction energies were estimated using Lennard-Jones potentials,[8] and the calculated E_{vdw} values were similar for all these structures within each given zeolite framework, indicative of their similar confinement effects for all these transformations. More specifically, these calculations show that each confining host framework stabilizes the $24DMP^=$ isomerization and β-scission transition states to the same extent. These findings are consistent with previous assessments of primary and secondary events for nC_7 reactions during transient desorption of NH_3 titrants on FAU, SFH, BEA, and MFI (seven samples of varying $R^2\rho_{H^+}$ values).[8] Such reaction-transport formalisms, and the similar product selectivities obtained by extrapolation to low ρ_{H^+} during titrant desorption ($\chi(t) \rightarrow 0$) for each product on large-pore FAU, SFH, and BEA zeolites, demonstrate that the nature of the zeolite framework does not detectably influence intrinsic (single-sojourn) selectivities on protons in aluminosilicates.

The theoretical and experimental evidence against confinement effects on selectivity for these reactions was also examined for medium-pore aluminosilicate frameworks and specifically for MFI structures with a range of $R^2\rho_{H^+}$ values,[8] leading to the expectation that product selectivities extrapolated to low ρ_{H^+} during titrant desorption ($\chi(t) \rightarrow 0$) would also be similar on all medium-pore zeolites (MEL, MFI, and SVR). In contrast with these expectations, medium-pore zeolites gave detectable nC$_7$ selectivities (Figure 8; 0.01−0.04) and higher β-scission selectivities (Figure 8; 0.08−0.11 vs 0.026−0.028 for large-pore materials) and lower 23DMP selectivities (Figure 8; 0.20−0.75 vs 0.86−0.92 for large-pore materials) than large-pore aluminosilicates as ρ_{H^+} approaches zero.

The single-sojourn character of these selectivities extrapolated to zero ρ_{H^+} ($\chi(t) \rightarrow 0$) during NH$_3$ desorption on medium-pore zeolites was confirmed by comparing extrapolated selectivity values on MFI-1 and MFI-2, which vary 10-fold in their $R^2\rho_{H^+}$ values, and steady-state selectivities on (Na)MFI-2, MFI-2 which had 99% of its protons titrated with Na (Section 2.1). These MFI-1, MFI-2, and (Na)MFI-2 samples gave nearly the same extrapolated selectivities to each product (Figure 8; ∼0.55, ∼0.34, ∼0.09, and ∼0.02, for MH, 23DMP, β-scission, and nC$_7$ selectivities, respectively), and as a result, such products are expected to reflect only those that form in a single reactive sojourn. Selectivities extrapolated to zero ρ_{H^+} ($\chi(t) \rightarrow 0$) during NH$_3$ desorption on medium pore zeolites SVR and MEL should also reflect only single reactive events. Such selectivities (extrapolated to zero ρ_{H^+} ($\chi(t) \rightarrow 0$) during NH$_3$ desorption) on SVR, a framework with similarly sized channels to those in MFI (0.47 nm[52]) but smaller channel intersections (0.59 nm for SVR vs 0.64 nm for MFI[52]), were greater for 23DMP (Figure 8; 0.64) and smaller for all other products (Figure 8; 0.27, 0.08, and 0.02, for MH, β-scission, and nC$_7$ selectivities, respectively). Extrapolated selectivities on MEL, whose channels (0.52 nm vs 0.47 nm for MFI[52]) and intersections (0.77 nm vs 0.64 nm for MFI[52]) are both larger than those for MFI, are conversely smaller for 23DMP (Figure 8; 0.19) and greater for all other products (Figure 8; 0.61, 0.1, and 0.03, for MH, β-scission, and nC$_7$ selectivities, respectively).

These data illustrate the ubiquitous role of diffusional effects, which cause a secondary reactions to occur within domains in which the chemical potential of the alkenes formed is higher than in regions outside of such domains. These domains often consist of porous crystallites of size, void structure, and proton density and reactivity to maintain such gradients; in such cases, secondary products show trends that, when improperly interpreted, would lead to the conclusion that they form in single-sojourn effects. These diffusion-limited events may even involve a single cage-like structure in frameworks that exhibit undulations in their channels, and their apertures are small enough to impede egress of molecules formed through effective van der Waals contacts with transition states within the larger regions of such undulations. The latter effects cannot be described by continuum-type diffusion-reaction treatments because they involve a limited number of diffusive encounters with a single proton. These single cages are evident in medium-pore zeolites with undulating void environments created by the intersections of their 10-MR channels (MEL, SVR, MFI); they occur even in the absence of gradients over the crystal dimensions, as shown from the presence of secondary products even as ρ_{H^+} and $\chi(t)$ approach zero (Figure 8). These phenomena cause secondary reactions to occur within a single "cage", in a manner that is reminiscent of systems in which radical intermediates become "caged" within local regions in liquids and undergo multiple secondary reactions before they egress to the next solvent cage.[53,54] Their prevalence reflects the size of the cages and of the apertures through an undulation parameter that provides a metric that compares the sizes of the molecules that can form and the apertures through which they must egress.

Figure 9a shows the sizes of the smallest connecting apertures (pore-limiting diameter; d_{PL}) and of the largest intervening cavities (d_{LC}) along diffusive paths for different frameworks derived from probes of the void space based on spherical constructs.[55] Al-MCM-41, SFH, and BEA values lie along the parity line in Figure 9a, indicative of the absence of local cage-like environments. MFI, MEL, SVR, and FAU have d_{PL} values smaller than their d_{LC} values, consistent with an undulating diffusion path, thus making

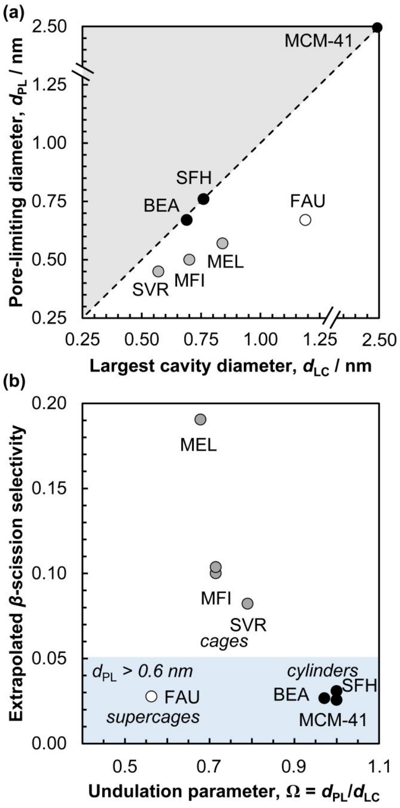

Figure 9. (a) Zeolite framework pore-limiting diameter, d_{PL}, plotted as a function of largest cavity diameter, d_{LC}.[55] The dashed line represents parity and thus the presence of cylindrical channels. (b) β-Scission selectivities, extrapolated to zero accessible protons during NH$_3$ desorption on each zeolite, and at steady-state for MCM-41, as a function of the undulation parameter (Ω, eq 21 of the main text), of the aluminosilicate. The shaded region represents large-pore aluminosilicates (d_{PL} >0.6 nm).

$$\Omega = d_{PL}/d_{LC} \tag{22}$$

the appropriate metric of such undulations.[56] The Ω values are 0.56−0.78 for MFI, MEL, SVR, and FAU, consistent with their cage-window motifs; these are created in the case of MFI, MEL, and SVR by the intersections of 10-MR cylindrical channels and by connected sodalite units in the case of FAU.

Figure 9b shows β-scission selectivities as $\chi(t)$ and ρ_{H^+} values approach zero on zeolites (and as bed residence times approach zero on Al-MCM-41) as a function of the Ω value of each framework. Frameworks with nearly cylindrical voids (Ω = 1; Al-

MCM-41, SFH, BEA) or with cages connected by large apertures ($d_{PL} > 0.6$ nm; FAU) show similar and low β-scission selectivities (0.025−0.028); they also do not form nC$_7$ isomers as products at low ρ_{H^+} values (or short bed residence times for Al-MCM-41). β-Scission selectivities on SVR, MFI, and MEL, however, increase as the framework Ω values decrease and undulations become more pronounced (β-scission selectivity = 0.08, 0.10, 0.19 and Ω = 0.78, 0.71, 0.68 for SVR, MFI, and MEL, respectively). The measured nC$_7$ selectivities (extrapolated to zero ρ_{H^+}) also increase with decreasing Ω values (Figure 8, nC$_7$ selectivity = 0.017, 0.020, 0.033 on SVR, MFI, and MEL, respectively), in spite of the secondary nature of nC$_7$ isomers in 24DMP reactions (Scheme 1b). Such extrapolated β-scission and nC$_7$ selectivities and the prevalence of these products in undulating void structures must reflect the possibility of multiple reactive events within a single cage. For example, 24DMP$^=$ converts to 23DMP$^=$ in a facile isomerization event, but its egress is delayed by the cage-window zeolite structure, which has larger voids well-suited to solvate formation transition states but smaller windows that impede alkene passage to the next cage. 23DMP alkenes are as reactive as 24DMP alkenes but diffuse even more slowly,[57] thus becoming “trapped” within a single cage until undergoing subsequent conversions into products that can readily egress (MH, nC$_7$, or β-scission products), either directly or by first re-forming the reactant alkene.

These single-cage events reflect the occurrence of several reactive events in the timescale of intercage passage and the facile formation of species within cages that diffuse slowly through the smaller interconnecting apertures. Such sequential transformations can thus occur in a single “visit” to a cage and even in the absence of gradients at the crystallite diameter scale, for which continuum diffusion-reaction models are appropriate and accurate. These cage-scale events find precedents in the ubiquitous β-scission of alkene oligomerization products on undulating frameworks,[56] which can form oligomers that diffuse slowly through connecting apertures but which exit the cage-like local structure only after β-scission events form smaller alkenes with higher intercage diffusivities.

These single-cage phenomena preclude the detection of those products formed in a single reactive sojourn of a reactant alkene at a proton; as a result, intrinsic selectivities on Al-MFI cannot be extracted from measured values using continuum diffusion-reaction treatments. Insights can be garnered from measured intrinsic selectivities on mesoporous and large-pore aluminosilicates because of the similar stabilization by confinement of 24DMP β-scission and isomerization transition states within FAU, SFH, BEA, and MFI (both cages and intersections), which was previously examined using theoretical methods and confirmed by similar van der Waals interaction energies derived from Lennard-Jones potentials for each given zeolite framework.[8] We surmise based on such an absence of preferential van der Waals stabilization of these transition states, taken together with the similar strength of acid sites in aluminosilicates, that β-scission selectivities on FAU, SFH, and BEA (extrapolated to zero $\chi(t)$ and ρ_{H^+}) and on Al-MCM-41 (extrapolated to zero bed residence time) represent the intrinsic values for all aluminosilicate acids, including the MFI framework materials for which single-cage events preclude the detection of the products formed in single sojourns.

Intracrystalline gradients become less severe, and diffusion-enhanced secondary reactions (and single-cage events) become less prevalent as the reactivity of protons decreases, for instance by the presence of weaker acid sites, because of a concomitant decrease in the Thiele moduli for product alkenes (eq 13). X-MFI (X = Ga, Fe, and B) materials give nC$_7$ isomerization first-order rate constants ($k_{isom,nC_7}K_{prot,nC_7}K_{dehyd,nC_7}$, eq 10) that are of strict kinetic origins and much smaller (by factors of 10−1000) than for Al-MFI (Figure 3; Al-MFI rate constants also of strict kinetic origins (Section 3.1 and previous work[8])) because of their less stable conjugate anions (as discussed in Section 3.1). Thiele moduli for product alkenes are thus at least 10−1000-fold smaller on Ga, Fe, and B-MFI zeotypes than on Al-MFI materials. As a result, measured selectivities on Ga, Fe, and B-MFI zeotypes are expected to reflect predominantly single-sojourn events with much smaller contributions from single-cage events.

Indeed, nC$_7$ products, which are formed only in secondary reactions of primary isomers and act as indicators of diffusion-enhanced secondary reactions or single-cage events, on these MFI zeotypes are undetectable, in contrast with their nonzero values (∼0.02) on Al-MFI. Such findings confirm that selectivities on these Ga-, Fe-, and B-MFI zeotypes reflect intrinsic primary values, without contributions from the single-cage events prevalent for the stronger acid sites in Al-MFI. In the next section, these intrinsic selectivities and how they are affected by acid strength are mechanistically assessed.

3.3. Consequences of Acid Strength on 2,4-Dimethylpentane Reaction Selectivity.

Intrazeolite 24DMP$^=$ concentration gradients preclude direct inquiries into the elementary steps involved in such transformations from measured rates. Reaction-transport models and measured rate constants together suggest the presence of severe 24DMP$^=$ concentration gradients in all materials except B-MFI is presented in the SI (section S6). As a result, direct experimental assessments of the effects of acid strength on X-MFI samples are infeasible for 24DMP reaction rates. Intrinsic product selectivities derived from NH$_3$ desorption experiments during catalysis (Section 3.2) for aluminosilicates and during steady-state reaction from X-MFI can be used to assess the effects of acid strength on the relative rates of the various concurrent reactions. These intrinsic product selectivities reflect relative rates that are strictly kinetic in origin, as discussed next using reaction-transport formalisms.

24DMP consumption reactions (primary isomerization and β-scission reactions; Scheme 2b) and nC$_7$ isomerization (Scheme 2a) are mediated by similar sets of elementary steps, and their rate equations share a similar functional form (eq 9). These steps are illustrated in Scheme 2b for the conversion of a 2,4-dimethylpentoxide attachment isomer to specific 2,3-dimethylpentoxide or propoxide attachment isomers, but they are involved in the conversion of all 2,4-dimethylpentoxide attachment isomers to all product alkoxides. 24DMP converts on the extracrystalline metal function to a quasi-equilibrated mixture of 2,4-dimethylpentenes (2,4-dimethylpent-2-ene shown as the illustrative example in Scheme 2b, Step 1) that are protonated in quasi-equilibrated steps to form 2,4-dimethylpentoxides (2,4-dimethylpent-2-oxide in Scheme 2b, Step 2). The 2,4-dimethylpentoxide attachment isomers then undergo skeletal isomerization (2,4-dimethylpent-2-oxide to 2,3-dimethylpent-4-oxide in Scheme 2b, Step 3a) or C−C bond cleavage (2,4-dimethylpent-2-oxide to isobutene and prop-2-oxide in Scheme 2b, Step 3b) in the kinetically relevant steps. The alkoxides formed desorb via β-hydrogen elimination to form product alkenes and regenerate protons (2,3-dimethylpent-4-oxide to 2,3-dimethylpent-4-ene in Scheme 2b, Step 5a; prop-2-oxide to propene in Scheme 2b, Step 5b). These alkene products diffuse through the acid domain and are hydrogenated to their less saturated analogues (2,3-dimethylpent-4-ene to 2,3-dimethylpentane (23DMP) in Scheme 2b, Step 5a, isobutene and propene to isobutane and propane in Scheme 2b, Step 5b) on the extracrystalline Pt function. These elementary steps, taken together with bare protons and 2,4-dimethylpentoxides as MASI, give the rate equation

$$\frac{r_{\mathrm{total},24}}{[\mathrm{H}^+]} = \frac{k_{\mathrm{total},24}K_{\mathrm{prot},24}K_{\mathrm{dehyd},24}(24\mathrm{DMP}/\mathrm{H}_2)}{1 + K_{\mathrm{prot},24}K_{\mathrm{dehyd},24}(24\mathrm{DMP}/\mathrm{H}_2)} \tag{23}$$

where 24DMP conversion rates ($r_{\mathrm{total},24}$) reflect the combined rates of β-scission ($r_{\beta,24}$) and isomerization (to each measured product isomer, j; $r_{\mathrm{isom},24,j}$) events:

$$r_{\mathrm{total},24} = r_{\beta,24} + \sum_j r_{\mathrm{isom},24,j} \tag{24}$$

$K_{\mathrm{dehyd},24}$ is the equilibrium constant for dehydrogenation of 24DMP to an equilibrated mixture of 2,4-dimethylpentene regioisomers; $K_{\mathrm{prot},24}$ is the equilibrium constant for formation of equilibrated attachment isomers of 2,4-dimethylpentoxides (24DMP*) from $24\mathrm{DMP}^{=}$; and $k_{\mathrm{total},24}$ is given by

$$k_{\mathrm{total},24} = k_{\beta,24} + k_{\mathrm{isom},24} \tag{25}$$

The $k_{\beta,24}$ and $k_{\mathrm{isom},24}$ terms account for all C−C bond cleavage and skeletal isomerization events of all 2,4-dimethylpentoxide attachment isomers, respectively.

The form of the rate expression in eq 23 can be regressed to the measured rate data, in spite of intracrystalline $24\mathrm{DMP}^{=}$ concentration gradients (reaction-transport formalisms discussed in the SI, section S6). These regressed first-order parameters (denoted as $\psi_{\mathrm{total},24}$, $\psi_{\mathrm{isom},24}$, and $\psi_{\beta,24}$ for total, isomerization, and β-scission parameters, respectively) are given by

$$\psi_{\mathrm{total},24} = \Gamma_{24}k_{\mathrm{total},24}K_{\mathrm{prot},24}K_{\mathrm{dehyd},24} \tag{26a}$$

$$\psi_{\mathrm{isom},24} = \Gamma_{24}k_{\mathrm{isom},24}K_{\mathrm{prot},24}K_{\mathrm{dehyd},24} \tag{26b}$$

$$\psi_{\beta,24} = \Gamma_{24}k_{\beta,24}K_{\mathrm{prot},24}K_{\mathrm{dehyd},24} \tag{26c}$$

for first-order reactions on quasi-spherical crystallites. Γ_{24} is the effectiveness factor, as defined in eq 14; it represents the ratio of measured to kinetic rate constants for a given reaction and is an indication of the severity of reactant concentration gradients.

Intrinsic β-scission and primary isomerization (to 23DMP, 2MH, and 3MH) selectivities can thus be expressed as ratios of $\psi_{\mathrm{isom},24}$ and $\psi_{\beta,24}$ values:

$$\frac{S_{24,\beta,0}}{S_{24,\mathrm{isom},0}} = \frac{\psi_{\beta,24}k_{\beta,24}K_{\mathrm{prot},24}K_{\mathrm{dehyd},24}}{\psi_{\mathrm{isom},24}k_{\mathrm{isom},24}K_{\mathrm{prot},24}K_{\mathrm{dehyd},24}} \tag{27}$$

Here, $S_{24,\beta,0}$ and $S_{24,\mathrm{isom},0}$ denote the intrinsic product selectivities (defined by eq 5). The value of Γ_{24} is identical for the parallel isomerization and β-scission pathways because both reactions involve the same 24DMP* species in equilibrium with local $24\mathrm{DMP}^{=}$ concentrations (SI, section S6). Equation 27 thus simplifies to

$$\frac{S_{24,\beta,0}}{S_{24,\mathrm{isom},0}} = \frac{k_{\beta,24}K_{\mathrm{prot},24}K_{\mathrm{dehyd},24}}{k_{\mathrm{isom},24}K_{\mathrm{prot},24}K_{\mathrm{dehyd},24}} \equiv \omega \tag{28}$$

These intrinsic selectivities ($S_{24,\beta,0}$ and $S_{24,\mathrm{isom},0}$) were determined in Section 3.2 for aluminosilicates by extrapolation to zero intracrystalline residence times (as $\rho_{\mathrm{H}+}$ and $\chi(t)$ values approached zero, varied by desorption of NH_3 during 24DMP reactions); such methods are required because primary product alkenes undergo secondary reactions in the same acid domains in which they first form. These diffusional enhancements of secondary reactions arise because the acid sites in these materials confer high reactivity to protons, a result of both the stability of the conjugate anion and of the van der Waals stabilization conferred by voids of molecular dimensions because product alkenes also diffuse slowly through the small pores and voids of these materials. The selectivities on weaker acids (X-MFI zeotypes, where X = Ga, Fe, and B) are unaffected by secondary reactions that occur on either the lengthscale of crystallites or single cages (as discussed in detail in Section 3.2).

The ω values on X-MFI samples are shown in Figure 10 as a function of the DPE of each solid acid, used here as the rigorous measure of acid strength. These ω values increase by 8-fold as acids weakened (DPE increases), in contrast with isomerization selectivities (rate ratios) that did not vary with acid strength (Section 3.1). These data indicate that β-scission transition states are destabilized to a lesser extent than isomerization transition states as the conjugate anions become less stable and that such weaker acids, in fact, favor β-scission over isomerization events.

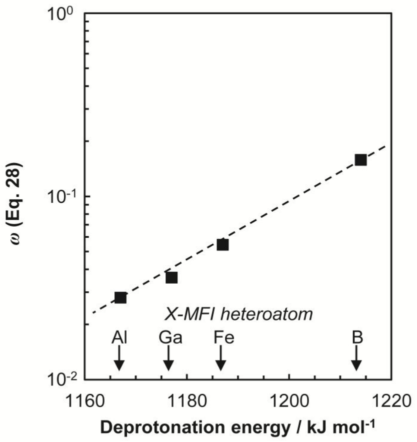

Figure 10. 2,4-Dimethylpentane β-scission and isomerization rate constant ratios (ω, eq 28) as a function of X-MFI deprotonation energy (X = Al, Ga, Fe, B) (548 K). The dashed line represents the regressed exponential fit of these rate constant ratios as a function of DPE (eq 31).

These selectivity trends can be assessed using Born−Haber thermochemical cycles that seek to describe the relevant free energies responsible for these selectivity ratios in terms of convenient hypothetical steps that decouple the relevant properties of the solid from those of the molecules involved (Scheme 5). The ω values reflect differences in free energies between the ensembles of transition states for β-scission and isomerization reactions

$$\begin{aligned}\omega &= \exp\left(-\left(\frac{\Delta G^{\ddagger}_{\beta}}{k_{\mathrm{B}}T} - \sum_j \frac{\Delta G^{\ddagger}_{\mathrm{isom},j}}{k_{\mathrm{B}}T}\right)\right)\\ &= \exp\left(-\left(\frac{\Delta G^{\ddagger}_{\beta}}{k_{\mathrm{B}}T} - \frac{\langle\Delta G^{\ddagger}_{\mathrm{isom}}\rangle}{k_{\mathrm{B}}T}\right)\right) = \exp\left(-\frac{\langle\Delta\Delta G^{\ddagger}\rangle}{k_{\mathrm{B}}T}\right)\end{aligned} \tag{29}$$

Scheme 5. Thermochemical Cycles That Deconstruct Activation Barriers for Acid-Catalyzed 2,4-Dimethylpentene Isomerization and β-Scission Reactions Represented Using Sequences of Hypothetical Steps[a]

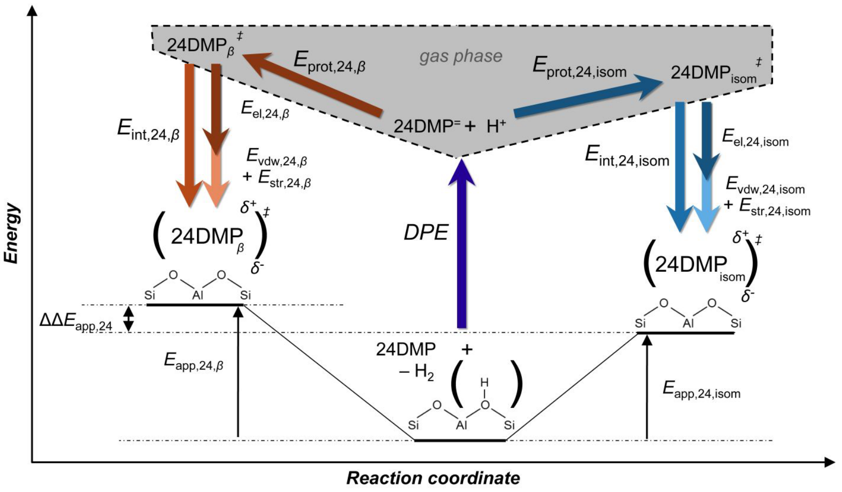

[a]Activation energies reflected in the first-order rate constants ($E_{app,24,isom}$ and $E_{app,24,\beta}$ for isomerization and β-scission, respectively) and in their ratios (ω, eq 30; $\Delta\Delta E_{app,24}$) are indicated.

where j indicates primary isomer product j and $\Delta G^‡_\beta$ and $\Delta G^‡_{isom,j}$ are the activation free energies of the ensembles of 24DMP$^=$ β-scission transition states and isomerization (to j) transition states, respectively. $\langle\Delta\Delta G^‡\rangle$ represents the difference in the free energy difference between $\Delta G^‡_\beta$ and $\langle\Delta G^‡_{isom}\rangle$. At the moderate temperatures (548 K) of 24DMP isomerization and β-scission catalysis, eq 29 can be rewritten in terms of energies because entropic contributions to transition state free energies are similar for these monomolecular 24DMP$^=$ reactions and thus compensate for each other:

$$\omega = \exp\left(-\frac{\langle\Delta\Delta E_{app,24}\rangle}{k_B T}\right) \tag{30}$$

This difference in transition state energies ($\Delta\Delta E_{app,24} = E_{app,24,\beta} - E_{app,24,isom}$) is treated in terms of the thermochemical cycles in Scheme 5, analogous in construction to those for nC$_7$ isomerization (Scheme 4) and with steps chosen to dissect catalyst and molecular properties relevant to the relative rates of isomerization and β-scission and isomerization of 24DMP.

The sensitivity of ω values to changes in DPE is given by

$$-k_B T\frac{\partial(\ln(\omega))}{\partial(\mathrm{DPE})} = \frac{\partial(\langle\Delta\Delta E_{app,24}\rangle)}{\partial(\mathrm{DPE})} \tag{31}$$

for the case of activation entropies that are similar for 24DMP$^=$ isomerization and β-scission transition states; the line in Figure 10 represents the regression of these data to the functional form of this equation. The value of $\partial(\langle\Delta\Delta E_{app,24}\rangle)/\partial(\mathrm{DPE})$ (−0.11) is indicative of weak effects of DPE on the differences between β-scission and isomerization transition state energies, with β-scission transition states becoming energetically more favored than isomerization transition states on weaker acids.

The chemical origins of such effects of DPE on selectivity (devoid of any artifacts caused by diffusional enhancements of secondary β-scission reactions) become evident from DFT-derived transition state energies for 24DMP β-scission and isomerization. The lowest energy transition state within each transition state ensemble was isolated at the T20-O(12)H location in Al-MFI using functionals that account for dispersive interactions (Section 2.3). Such transition states were then isolated at this same location but with Ga, Fe, or B, instead of Al, as the heteroatoms. Figure 4b shows the structures of 24DMP$^=$ isomerization and β-scission transition state carbocations; their positive charges (δ^+ = 0.90−0.92 for isomerization, 0.74−0.76 for β-scission; Figure 4b) reflect the nearly complete transfer of the proton to the organic moiety at the transition state. Figure 11 shows DFT-derived $\langle\Delta\Delta E_{app,24}\rangle$ values as a function of DPE on these X-MFI structures (carbocation structures in Figure 4b). The slope of these DFT-derived values with DPE ($\partial(\langle\Delta\Delta E_{app,24}\rangle)/\partial(\mathrm{DPE})$ = −0.13) is in excellent agreement with measured values (−0.11; Figure 10).

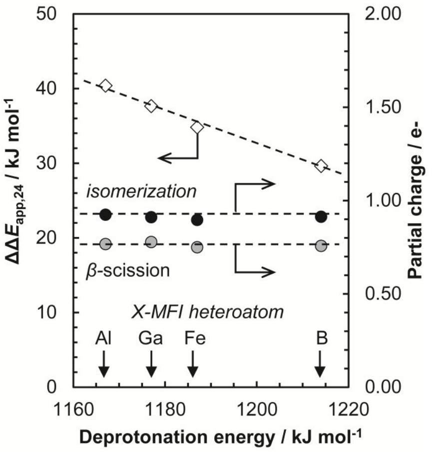

Figure 11. DFT-derived $\Delta\Delta E_{app,24}$ values ($E_{app,24,\beta} - E_{app,24,isom}$) (diamonds, left axis) and partial charges (Section 2.3) at transition state carbocations for 24DMP β-scission (gray circles, right axis) and isomerization (black circles, right axis) as a function of deprotonation energy on MFI zeotypes of different strength (RPBE PAW D3(BJ); MFI T12-O(20)H). Dashed lines represent the linear fit for energies and the average value for charges.

DOI: 10.1021/acs.jpcc.8b08460
J. Phys. Chem. C 2018, 122, 25475−25497

The preferential stabilization of isomerization transition states over those involved in β-scission with increasing acid strength can be interpreted using the formalism of the thermochemical cycles in Scheme 5, as discussed previously for $n\mathrm{C}_7$ isomerization (Scheme 4). The relevant energy difference for ω values is that between the transition states that mediate these respective reactions ($\langle\Delta\Delta E_{\mathrm{app},24}\rangle$). The specific hypothetical steps composing this thermochemical cycle are analogous to those discussed in detail for $n\mathrm{C}_7$ isomerization in Section 3.1. This thermochemical cycle leads to differences in activation barriers ($\langle\Delta\Delta E_{\mathrm{app},24}\rangle$) given by

$$\langle\Delta\Delta E_{\mathrm{app},24}\rangle = \langle\Delta E_{\mathrm{prot},24}\rangle + \langle\Delta E_{\mathrm{es},24}\rangle + \langle\Delta E_{\mathrm{vdw},24}\rangle + \langle\Delta E_{\mathrm{str},24}\rangle \tag{32}$$

The sensitivity of ω values to DPE is given by the derivative of eq 32 with respect to DPE:

$$\frac{\partial(\langle\Delta\Delta E_{\mathrm{app},24}\rangle)}{\partial(\mathrm{DPE})} = \frac{\partial(\langle\Delta E_{\mathrm{es},24}\rangle)}{\partial(\mathrm{DPE})} + \frac{\partial(\langle\Delta E_{\mathrm{vdw},24}\rangle)}{\partial(\mathrm{DPE})} + \frac{\partial(\langle\Delta E_{\mathrm{str},24}\rangle)}{\partial(\mathrm{DPE})} \tag{33}$$

In this equation, the derivatives of proton affinity terms (E_{prot}) are zero because such energies are properties of gaseous molecular species and thus unaffected by solid acid properties such as DPE. The contributions from the van der Waals components (E_{vdw}) and structural framework deformations (E_{str}) can be assessed using DFT-derived structures and energies for the relevant transition states and Lennard-Jones potentials to estimate van der Waals interaction energies between the transition state carbocations and the confining framework voids.

24DMP isomerization and β-scission transition state carbocations are similar in size and shape (structures in Figure 4b) and are stabilized to similar extents by each confining void, as shown by their similar van der Waals interaction energies derived from Lennard-Jones potentials.[8] Transition state carbocations for isomerization (24DMP$^=$-23DMP$^=$) and 24DMP$^=$ β-scission are held at similar distances away from conjugate anions (ion-pair transition state distances given in section S4, SI), irrespective of DPE; consequently, E_{vdw} and E_{str} values are insensitive to acid strength, and eq 33 can be simplified to

$$\frac{\partial\langle\Delta\Delta E_{\mathrm{app},24}\rangle}{\partial\mathrm{DPE}} = \frac{\partial\langle\Delta E_{\mathrm{el},24}\rangle}{\partial\mathrm{DPE}} \tag{34}$$

This equation attributes changes in ω values with DPE to differences in electrostatic interaction energies between isomerization and β-scission ion-pair transition states.

The charges in each of these two transition state carbocation structures do not vary with DPE ($\delta^+ = \sim0.91$ for isomerization, ~0.75 for β-scission; Figure 11). As in the case of $n\mathrm{C}_7$ isomerization transition states (Section 3.1), both of these ion-pair transition states are stabilized predominantly by electrostatic interactions between the cationic and anionic moieties at the transition state; these electrostatic interactions depend on the amount and extent of delocalization of charges at the two different carbocations involved in the isomerization and β-scission transition states because the negative charges on conjugate anions are highly localized near the heteroatoms in both cases as a result of the insulating nature of the zeotype framework.[7]

Figure 4b shows the structures and charge distributions for the carbocation moieties at isomerization and β-scission transition states. β-Scission transition states are slightly less charged than isomerization transition states ($\delta^+ = 0.75$ vs 0.89 for β-scission and isomerization, respectively). The β-scission transition state carbocation is composed of an isobutene leaving group that is only slightly positively charged ($\delta^+ = 0.15$) and an alkyl fragment (a positively charged propenium ion) that forms prop-2-oxide (Scheme 2b, Step 3b). This transition state places most of the positive charge on the central C atom of the propenium ion ($\delta^+ = 0.35$), with the two methyl substituents at this C atom exhibiting a small positive charge ($\delta^+ = 0.13$ each), as expected from their electron donation to the central carbon. In contrast, the isomerization transition state delocalizes charge throughout its cyclopropyl carbenium ion backbone, with the two C atoms vicinal to the conjugate anion bearing nearly half of the positive charge of the organic cation (Figure 4b; $\delta^+ = 0.40$). The additional alkyl substituents on the backbone delocalize only small amounts of charge ($\delta^+ = 0.00$−0.12 each). These differences in delocalization of positive charge result in different Coulombic interactions with conjugate anions. 24DMP$^=$ isomerization transition states highly delocalize positive charge that prevent their effective recovery of DPE. β-Scission transition states, with their highly localized charge, recover more of the charge required to deprotonate a weaker acid (relative to isomerization transition states). Their activation barriers thus are less affected by less stable conjugate anions than those for isomerization, resulting in β-scission selectivities that increase for weaker acids.

These findings are consistent with acid strength effects for C_6 alkene isomerization[51] and methylcyclohexene ring contraction[11] on stronger mesoporous solid acids of varying strength (Keggin-type polyoxometalate clusters of varying central atom, DPE = 1087−1143 kJ mol^{-1}, supported on SiO_2). First-order rate constants for C_6 alkene isomerization decreased less sensitively with increasing DPE than those for methylcyclohexene ring contraction ($\frac{\mathrm{d}(\ln(k_{\mathrm{first}}))}{\mathrm{d(DPE)}} = 0.11$ and 0.19 for C_6 alkene isomerization and methylcyclohexene ring contraction, respectively).

The alkyl-substituted cyclopropyl carbenium ions (mediating C_6 alkene isomerization) and alkyl-substituted bicyclo[3.1.0]-hexyl carbenium ions (mediating methylcyclohexene ring contraction) did not recover the same fraction of DPE. The double-ring structure of the ring contraction transition state carbocations delocalizes positive charge more effectively than the alkyl substituents of alkene isomerization transition states. Such a highly dispersed positive charge results in less effective Coulombic interactions at ion-pair transition states, compared to those in alkene isomerization transition states; consequently, ring contraction transition states recover a smaller fraction of deprotonation energy than isomerization transition states for each acid.

The combined experimental and theoretical approach in this work has demonstrated that weaker acids preferentially stabilize β-scission transition states over isomerization transition states, in contradiction to prevalent paradigms.[12−15] In fact, the phenomenological observation that stronger acids preferentially perform β-scission largely reflects contributions from diffusional enhancements of secondary reactions, which result in the secondary conversion of primary product alkenes within the same acid domains where they first formed. Such diffusional enhancements occur on length scales of zeolite and zeotype crystallites and can also arise as a result of cage-window framework structures (Section 3.2); in such undulating frameworks, even single-site selectivities include contributions from multiple reactions at a single proton. This reaction–transport coupling is here the result of the small pores and voids of zeolites, which not only stabilize transition states through van der Waals interactions and thus confer high reactivity to protons but also sensitively determine molecular diffusivities of reactants and products; the entanglement of reactive and diffusive phenomena is ubiquitous in heterogeneously catalyzed reactions, and their effects must be carefully addressed.

4. CONCLUSIONS

The catalytic consequences of acid strength on reactivity and selectivity for alkane isomerization and β-scission reactions were addressed here using physical mixtures of Pt/SiO_2 and MFI-framework zeotypes (X-MFI, where X = Al, Ga, Fe, and B), microporous solid acids with acid sites that differ in acid strength (DPE = 1167−1214 kJ mol^{-1}) but that reside within the same small pores and voids. *n*-Heptane isomerization (to methylhexane products) rate constants decreased with increasing DPE, primarily reflecting the decrease in stability of the conjugate anion present at the ion-pair transition states that mediate these reactions; first-order rate constants (per H^+) reflect the free energy difference between these transition states and their neutral gas-phase *n*-heptane and H_2 precursors, together with bare protons. The sensitivity of *n*-heptane isomerization rate constants to DPE reflects transition state ion pairs that recover energy through Coulombic interactions but are essentially unable to recover the energy required for charge reorganization upon heterolytic cleavage of O−H bonds at the acid sites.

The charge distributions are similar for all alkyl-substituted cyclopropyl carbenium ions mediating primary and secondary isomerization events in *n*-heptane isomerization, resulting in their similar electrostatic interactions with conjugate anions of a given strength; as a result, their sensitivity to changes in acid strength is similar, and their selectivities are constant values that reflect differences in proton affinity among these carbenium ions but that are independent of DPE. In contrast, the positive charge for β-scission transition state carbocations is more localized than for isomerization transition state carbocations, resulting in effective electrostatic interactions with the localized negative charge at the conjugate anions of these insulating materials; β-scission transition state energies are thus less sensitive to changes in acid strength than are isomerization transition states.

Experimental assessment of β-scission and isomerization selectivities, both primary pathways available to 2,4-dimethylpentane reactants, first required the dissection of measured selectivities into their intrinsic (single-sojourn) values and the contributions from the diffusional enhancements of secondary reactions. Rigorous reaction-transport formalisms demonstrate that these diffusional constraints become more severe on protons of higher reactivity, acid domains of larger size and proton density, and zeolite frameworks that restrict molecular diffusion. These mathematical treatments, together with product selectivities measured during the desorption of preadsorbed NH_3 titrants, demonstrated that intrinsic selectivities during 2,4-dimethylpentane reactions were independent of zeolite topology, at least for large-pore and mesoporous aluminosilicates; medium-pore materials with undulations in their frameworks, however, resulted in the diffusional enhancement of secondary reactions on the lengthscale of a single cage and proton. These cage effects reflected not differences in intrinsic selectivities but only the breakdown of the continuum approximation on these lengthscales.

The ratio of β-scission to isomerization selectivities during 2,4-dimethylpentane reactions reflects kinetic rate constant ratios, in spite of the presence of kinetically relevant 2,4-dimethylpentene concentration gradients in acid domains. These selectivity ratios on MFI-framework zeotypes increase with decreasing acid strength, indicating that β-scission transition states are less sensitive to weaker acids than are isomerization transition states. Such findings are in contrast to the prevalent requirement for stronger acid sites to preferentially catalyze β-scission reactions. In fact, these reported selectivity trends merely reflect the severe diffusional constraints imposed by stronger acids, with acid sites of higher intrinsic reactivity.

■ ASSOCIATED CONTENT

Ⓢ Supporting Information

The Supporting Information is available free of charge on the ACS Publications website at DOI: 10.1021/acs.jpcc.8b08460.

> Derivation of *n*-heptane and 2,4-dimethylpentane isomerization and β-scission rate expressions, values of regressed rate parameters, transmission electron micrographs, bond distances and charges from DFT, product selectivities, and assessments of the presence and severity of 2,4-dimethylpentane reactant alkene concentration gradients (PDF)

■ AUTHOR INFORMATION

Corresponding Author

*E-mail: iglesia@berkeley.edu.

ORCID

Gina Noh: 0000-0003-4717-5767

Enrique Iglesia: 0000-0003-4109-1001

Notes

The authors declare no competing financial interest.

■ ACKNOWLEDGMENTS

The authors acknowledge financial support from the Chevron Energy Technology Company; technical discussion with Drs. William Knaeble (University of California, Berkeley) and Prashant Deshlahra (Tufts University); SVR synthesis and characterization by Dr. Tracy Davis (Chevron); and computational resources from the Extreme Science and Engineering Discovery Environment (XSEDE), supported by the National Science Foundation through grant number ACI-1053575 (research allocation CHE-140066). G.N. acknowledges a Chevron Fellowship granted in support of this research.

■ REFERENCES

(1) Ward, J. W. Design and preparation of hydrocracking catalysts. *Stud. Surf. Sci. Catal.* **1983**, *16*, 587−618.

(2) Miller, S. J. New molecular sieve process for lube dewaxing by wax isomerization. *Microporous Mater.* **1994**, *2*, 439−449.

(3) Heinemann, H.; Mills, G. A.; Hattman, J. B.; Kirsch, F. W. Houdriforming reactions: Studies with pure hydrocarbons. *Ind. Eng. Chem.* **1953**, *45*, 130−134.

(4) Coonradt, H. L.; Garwood, W. E. Mechanism of hydrocracking. Reactions of paraffins and olefins. *Ind. Eng. Chem. Process Des. Dev.* **1964**, *3*, 38−45.

(5) Weisz, P. B. Polyfunctional heterogeneous catalysis. *Adv. Catal.* **1962**, *13*, 137−190.

(6) Jones, A. J.; Carr, R. T.; Zones, S. I.; Iglesia, E. Acid strength and solvation in catalysis by MFI zeolites and effects of the identity,

concentration and location of framework heteroatoms. *J. Catal.* **2014**, *312*, 58−68.

(7) Deshlahra, P.; Iglesia, E. Toward more complete descriptors of reactivity in catalysis by solid acids. *ACS Catal.* **2016**, *6*, 5386−5392.

(8) Noh, G.; Shi, Z.; Zones, S. I.; Iglesia, E. Isomerization and β-scission reactions of alkanes on bifunctional metal-acid catalysts: Consequences of confinement and diffusional constraints on reactivity and selectivity. *J. Catal.* **2018**, DOI: 10.1016/j.jcat.2018.03.033.

(9) Jones, A. J.; Zones, S. I.; Iglesia, E. Implications of transition state confinement within small voids for acid catalysis. *J. Phys. Chem. C* **2014**, *118*, 17787−17800.

(10) Gounder, R.; Iglesia, E. The catalytic diversity of zeolites: confinement and solvation effects within voids of molecular dimensions. *Chem. Commun.* **2013**, *49*, 3491−3509.

(11) Knaeble, W.; Iglesia, E. Acid strength and metal-acid proximity effects on methylcyclohexane ring contraction turnover rates and selectivities. *J. Catal.* **2016**, *344*, 817−830.

(12) Park, K.; Ihm, S. Comparison of Pt/zeolite catalysts for n-hexadecane hydroisomerization. *Appl. Catal., A* **2000**, *203*, 201−209.

(13) Bi, Y.; Xia, G.; Huang, W.; Nie, H. Hydroisomerization of long chain n-paraffins: The role of the acidity of the zeolite. *RSC Adv.* **2015**, *5*, 99201−99206.

(14) Zhang, W.; Smirniotis, P. G. Effect of zeolite structure and acidity on the product selectivity and reaction mechanism for n-octane hydroisomerization and hydrocracking. *J. Catal.* **1999**, *182*, 400−416.

(15) Corma, A.; Martinez, A.; Pergher, S.; Peratello, S.; Perego, C.; Bellusi, G. Hydrocracking-hydroisomerization of n-decane on amorphous silica-alumina with uniform pore diameter. *Appl. Catal., A* **1997**, *152*, 107−125.

(16) Jones, A. J.; Iglesia, E. The strength of Brønsted acid sites in microporous aluminosilicates. *ACS Catal.* **2015**, *5*, 5741−5755.

(17) Rybicki, M.; Sauer, J. Acid strength of zeolitic Brønsted sites—Dependence on dielectric properties. *Catal. Today* **2018**, DOI: 10.1016/j.cattod.2018.04.031.

(18) Jackowski, A.; Zones, S. I.; Burton, A. W. A study on zeolite synthesis from diquaternary ammonium compounds; the effect of changing end-group heterocycles in the HF/SiO2 synthesis of molecular sieves. *Stud. Surf. Sci. Catal.* **2008**, *174*, 111−116.

(19) Terasaki, O.; Ohsuna, T.; Sakuma, H.; Watanabe, D.; Nakagawa, Y.; Medrud, R. C. *Chem. Mater.* **1996**, *8*, 463−468.

(20) Cejka, J.; Corma, A.; Zones, S. *Zeolites and Catalysis*; Wiley-VCH, 2010.

(21) Baertsch, C. D.; Komala, K. T.; Chua, Y.-H.; Iglesia, E. Genesis of Brønsted acid sites during dehydration of 2-butanol on tungsten oxide catalysts. *J. Catal.* **2002**, *205*, 44−57.

(22) Alberty, R. A.; Gehrig, C. A. Standard chemical thermodynamic properties of alkane isomer groups. *J. Phys. Chem. Ref. Data* **1984**, *13*, 1173−1197.

(23) Kresse, G.; Hafner, J. Ab initio molecular dynamics for liquid metals. *Phys. Rev. B: Condens. Matter Mater. Phys.* **1993**, *47*, 558−561.

(24) Kresse, G.; Hafner, J. Ab initio molecular-dynamics simulation of the liquid-metal−amorphous-semiconductor transition in germanium. *Phys. Rev. B: Condens. Matter Mater. Phys.* **1994**, *49*, 14251−14269.

(25) Kresse, G.; Furthmüller, J. Efficient iterative schemes for ab initio total-energy calculations using a plane-wave basis set. *Phys. Rev. B: Condens. Matter Mater. Phys.* **1996**, *54*, 11169−11186.

(26) Kresse, G.; Furthmüller, J. Efficiency of ab-initio total energy calculations for metals and semiconductors using a plane-wave basis set. *Comput. Mater. Sci.* **1996**, *6*, 15−50.

(27) Kresse, G. From ultrasoft pseudopotentials to the projector augmented-wave method. *Phys. Rev. B: Condens. Matter Mater. Phys.* **1999**, *59*, 1758−1775.

(28) Blöchl, P. E. Projector augmented-wave method. *Phys. Rev. B: Condens. Matter Mater. Phys.* **1994**, *50*, 17953−17979.

(29) Perdew, J. P.; Burke, K.; Ernzerhof, M. Generalized gradient approximation made simple. *Phys. Rev. Lett.* **1996**, *77*, 3865−3868.

(30) Yang, K.; Zheng, J.; Zhao, Y.; Truhlar, D. G. Tests of the RPBE, revPBE, τ-HCTHhyb, ωB97X-D, and MOHLYP density functional approximations and 29 others against representative databases for diverse bond energies and barrier heights in catalysis. *J. Chem. Phys.* **2010**, *132*, 164117.

(31) Grimme, S.; Antony, J.; Ehrlich, S.; Krieg, H. A consistent and accurate ab initio parametrization of density functional dispersion correction (DFT-D) for the 94 elements H-Pu. *J. Chem. Phys.* **2010**, *132*, 154104.

(32) Grimme, S.; Ehrlich, S.; Goerigk, L. Effect of the damping function in dispersion corrected density functional theory. *J. Comput. Chem.* **2011**, *32*, 1456−1465.

(33) Jónsson, H.; Mills, G.; Jacobsen, K. W. Nudged elastic band method for finding minimum energy paths of transitions. In *Classical and Quantum Dynamics in Condensed Phase Simulations Proceedings of the International School of Physics*; Berne, B. J., Ciccotti, G., Coker, D. F., Eds.; 1997; p 385..

(34) Henkelman, G.; Jónsson, H. A dimer method for finding saddle points on high dimensional potential surfaces using only first derivatives. *J. Chem. Phys.* **1999**, *111*, 7010−7022.

(35) Löwdin, P. On the non-orthogonality problem connected with the use of atomic wave functions in the theory of molecules and crystals. *J. Chem. Phys.* **1950**, *18*, 365−375.

(36) Qian, X.; Li, J.; Qi, L.; Wang, C. Z.; Chan, T. L.; Yao, Y. X.; Ho, K. M.; Yip, S. Quasiatomic orbitals for ab initio tight-binding analysis. *Phys. Rev. B: Condens. Matter Mater. Phys.* **2008**, *78*, 1−22.

(37) Chan, T. L.; Yao, Y. X.; Wang, C. Z.; Lu, W. C.; Li, J.; Qian, X. F.; Yip, S.; Ho, K. M. Highly localized quasiatomic minimal basis orbitals for Mo from ab initio calculations. *Phys. Rev. B: Condens. Matter Mater. Phys.* **2007**, *76*, 1−10.

(38) Lu, W. C.; Wang, C. Z.; Schmidt, M. W.; Bytautas, L.; Ho, K. M.; Ruedenberg, K. Molecule intrinsic minimal basis sets. I. Exact resolution of ab initio optimized molecular orbitals in terms of deformed atomic minimal-basis orbitals. *J. Chem. Phys.* **2004**, *120*, 2629−2637.

(39) Lu, W. C.; Wang, C. Z.; Chan, T. L.; Ruedenberg, K.; Ho, K. M. Representation of electronic structures in crystals in terms of highly localized quasiatomic minimal basis orbitals. *Phys. Rev. B: Condens. Matter Mater. Phys.* **2004**, *70*, 1−4.

(40) Olson, D. H.; Kokotailo, G. T.; Lawton, S. L.; Meier, W. M. Crystal structure and structure-related properties of ZSM-5. *J. Phys. Chem.* **1981**, *85*, 2238−2243.

(41) Van Koningsveld, H.; Van Bekkum, H.; Jansen, J. C. On the location and disorder of the tetrapropylammonium (TPA) ion in zeolite ZSM-5 with improved framework accuracy. *Acta Crystallogr., Sect. B: Struct. Sci.* **1987**, *43*, 127−132.

(42) Freysoldt, C.; Neugebauer, J.; Van de Walle, C. G. Electrostatic interactions between charged defects in supercells. *Phys. Status Solidi B* **2011**, *248*, 1067−1076.

(43) Huntley, D. R.; Markopoulos, G.; Donovan, P. M.; Scott, L. T.; Hoffmann, R. Squeezing C-C bonds. *Angew. Chem., Int. Ed.* **2005**, *44*, 7549−7553.

(44) Thiele, E. W. Relation between catalytic activity and size of particle. *Ind. Eng. Chem.* **1939**, *31*, 916−920.

(45) Fogler, H. S. *Elements of Chemical Reaction Engineering*, 4th ed.; Prentice Hall, 2005.

(46) Aronson, M.; Gorte, R. J.; Farneth, W. E. The influence of oxonium ion and carbenium ion stabilities on the alcohol/H-ZSM-5 interaction. *J. Catal.* **1986**, *98*, 434−443.

(47) Deshlahra, P.; Carr, R. T.; Iglesia, E. Ionic and covalent stabilization of intermediates and transition states in catalysis by solid acids. *J. Am. Chem. Soc.* **2014**, *136*, 15229−15247.

(48) Kramer, G. J.; van Santen, R. A. An ab initio study of D/H exchange between CD4 and the H-forms of zeolites FAU and MFI. *J. Am. Chem. Soc.* **1995**, *117*, 1766−1776.

(49) Olah, G. A. Stable carbocations. CXVIII. General concept and structure of carbocations based on differentiation of trivalent (classical) carbenium ions from three-center bound penta- of tetracoordinated (nonclassical) carbonium ions. Role of carbocations in electroph. *J. Am. Chem. Soc.* **1972**, *94*, 808−820.

(50) Natal-Santiago, M. A.; Alcalá, R.; Dumesic, J. A. DFT study of the isomerization of hexyl species involved in the acid-catalyzed conversion of 2-methyl-pentene-2. *J. Catal.* **1999**, *181*, 124−144.

(51) Knaeble, W.; Carr, R. T.; Iglesia, E. Mechanistic interpretation of the effects of acid strength on alkane isomerization turnover rates and selectivity. *J. Catal.* **2014**, *319*, 283−296.

(52) Baerlocher, C.; McCusker, L. Database of zeolite structures. http://www.iza-structure.org/databases/ (accessed June 18, 2018).

(53) Franck, J.; Rabinowitsch, E. Some remarks about free radicals and the photochemistry of solutions. *Trans. Faraday Soc.* **1934**, *30*, 120−130.

(54) Rabinowitch, E.; Wood, W. C. The collison mechanism and the primary photochemical process in solutions. *Trans. Faraday Soc.* **1936**, *32*, 1381−1387.

(55) First, E. L.; Gounaris, C. E.; Wei, J.; Floudas, C. A. Computational characterization of zeolite porous networks: an automated approach. *Phys. Chem. Chem. Phys.* **2011**, *13*, 17339−17358.

(56) Sarazen, M. L.; Doskocil, E.; Iglesia, E. Effects of void environment and acid strength on alkene oligomerization selectivity. *ACS Catal.* **2016**, *6*, 7059−7070.

(57) Xiao, J.; Wei, J. Diffusion mechanism of hydrocarbons in zeolites-II. Analysis of experimental observations. *Chem. Eng. Sci.* **1992**, *47*, 1143−1159.

DOI: 10.1021/acs.jpcc.8b08460